JGR Space Physics

RESEARCH ARTICLE
10.1029/2020JA028139

Special Section:
Solar and Heliospheric Plasma Structures: Waves, Turbulence, and Dissipation

Caltech Lab Experiments and the Insights They Provide Into Solar Corona Phenomena

Paul M. Bellan[1]

[1]Department of Applied Physics and Materials Science, California Institute of Technology, Pasadena, CA, USA

Abstract A comprehensive overview of two decades of Caltech experiments relevant to solar corona physics is presented. The extent to which the experiments scale to the solar corona, the basic configurations and operation, and the importance of the magnetic force $\mathbf{J} \times \mathbf{B}$ common to all the experiments is discussed. Summaries are given of the various configurations used, the main observations, and interpretations of these observations, including new models developed to provide these interpretations. Topics include observations and explanations for flux rope self-collimation, axial flows along flux ropes, eruption of arched flux ropes, strapping magnetic fields that inhibit eruption, the torus instability, and effects such as X-ray emission of a kink-driven secondary Rayleigh-Taylor instability.

Key Points:
- Lab experiments replicate main features of solar corona phenomena and provide a scale model
- Multiscale phenomena can be resolved
- Transition from MHD physics to kinetic physics can be resolved; new insights regarding how this works are obtained

Correspondence to:
P. M. Bellan,
pbellan@caltech.edu

Citation:
Bellan, P. M. (2020). Caltech lab experiments and the insights they provide into solar corona phenomena. *Journal of Geophysical Research: Space Physics*, *125*, e2020JA028139. https://doi.org/10.1029/2020JA028139

Received 28 APR 2020
Accepted 30 JUN 2020
Accepted article online 17 JUL 2020

1. Introduction

1.1. History and Motivation

Laboratory experiments on phenomena relevant to the solar corona began at Caltech in the mid-1990s. These experiments, an outgrowth of ongoing spheromak experiments, exploited the realization that spheromak physics is closely related to solar corona physics as both involve nonequilibrium magnetohydrodynamics (MHD), injection of magnetic helicity, and relaxation to minimum-energy states. Initial experiments had minimal diagnostics, and there was little understanding of how results could be scaled to the solar corona. With time, the experiments and diagnostics became more sophisticated, the scalability to the solar corona was understood, and models motivated by the experiment were developed and applied to the experiment and to the solar corona.

1.2. Benefits of Experiments

The traditional methods for studying the solar corona are observation, analytic models, and numerical models. Laboratory experiments provide a different and complementary approach. Unlike solar observations, laboratory experiments are repeatable with control of both initial and boundary conditions. Repeatability allows for scanning a single parameter to determine the dependence on that parameter. In contrast, the solar corona is neither repeatable nor controllable, so statistical methods must be used to determine parametric relationships. Analytic and numerical models necessarily involve simplifying assumptions, so significant physics is omitted. For example, analytic models typically focus on a small subset of the entire system by making restrictive assumptions about geometry, space scale, or timescale. While numerical models can characterize more complex geometry, numerical models have limited ability to characterize multiscale physics. By virtue of being real, laboratory experiments automatically involve no assumptions about physics, automatically involve realistic geometry, and automatically contain multiscale physics. However, care is required in relating laboratory experiments to the solar corona because some aspects of the experiments scale well to the solar corona, whereas others do not. The features that do not scale well are not necessarily irrelevant because consideration of these features stimulates understanding of how nonscalable but related phenomena might occur in the solar corona. Experiments often provide discovery of unexpected new phenomena, and these discoveries motivate development of new models that can then be immediately validated by further experiments.

2. Scalability to the Solar Corona

Because the ideal MHD equations have no intrinsic scale, laboratory experiments are relevant to the solar corona despite the approximately 5 to 8 orders of magnitude difference between time and length scales (microseconds and centimeters in the laboratory versus minutes and megameters for the solar corona).

A general method for scaling laboratory experiments to solar or even astrophysical situations was developed by Ryutov et al. (2000, 2001) who showed that two ideal MHD plasmas can be *directly* scaled to each other if they have the same reference $\beta_0 = \mu_0 P_0/B_0^2$. Here $P_0 = n_0 \kappa T_0$ and quantities with subscript 0 are reference values used for normalization. Scalability results because when the ideal MHD equations are expressed in dimensionless form, the only remaining parameter is β_0. Thus, for *any* reference mass density ρ_0, reference length l_0, and reference length B_0 *all* ideal MHD plasmas having the same β_0 are governed by a unique set of dimensionless equations, namely,

$$\bar{\rho}\left(\frac{\partial \overline{\mathbf{U}}}{\partial \bar{t}} + \overline{\mathbf{U}} \cdot \overline{\nabla}\,\overline{\mathbf{U}}\right) = \left(\overline{\nabla} \times \overline{\mathbf{B}}\right) \times \overline{\mathbf{B}} - \beta_0 \overline{\nabla} \overline{P} \tag{1a}$$

$$\frac{\partial \overline{\mathbf{B}}}{\partial \bar{t}} = \overline{\nabla} \times \left(\overline{\mathbf{U}} \times \overline{\mathbf{B}}\right) \tag{1b}$$

$$\frac{\partial \bar{\rho}}{\partial \bar{t}} + \overline{\nabla} \cdot \left(\bar{\rho}\,\overline{\mathbf{U}}\right) = 0 \tag{1c}$$

$$\left(\frac{\partial}{\partial \bar{t}} + \bar{U} \cdot \overline{\nabla}\right)\left(\overline{P}\,\bar{\rho}^{-\gamma}\right) = 0 \tag{1d}$$

where

$$\begin{aligned} v_{A0} &= \frac{B_0}{\sqrt{\mu_0 \rho_0}} \\ \tau_{A0} &= \frac{l_0}{v_{A0}} \\ \bar{\boldsymbol{x}} &= \frac{\boldsymbol{x}}{l_0} \\ \bar{t} &= \frac{t}{\tau_{A0}} \\ \overline{\nabla} &= l_0 \nabla \\ \bar{\rho} &= \frac{\rho}{\rho_0} \\ \overline{\boldsymbol{B}} &= \frac{\boldsymbol{B}}{B_0} \\ \overline{\boldsymbol{U}} &= \frac{\boldsymbol{U}}{v_{A0}} \\ \overline{P} &= \frac{P}{P_0} \end{aligned} \tag{2}$$

The crux of Ryutov's scaling method involves defining three parameters $c_1 = l_{0lab}/l_{0solar}$, $c_2 = \rho_{0lab}/\rho_{0solar}$, and $c_3 = P_{0lab}/P_{0solar}$ which then give the scaling from laboratory plasma to solar plasma parameters as

$$B_{solar} = \frac{B_{lab}}{\sqrt{c_3}},\ v_{A,\,solar} = v_{A,\,lab}\sqrt{\frac{c_2}{c_3}},\ \ \tau_{solar} = \frac{\tau_{lab}}{c_1}\sqrt{\frac{c_3}{c_2}} \tag{3}$$

Equation 3 shows that laboratory plasmas are scale models of solar plasmas to the extent that both are described by Equations 1a–1d. Table 1 lists reference and scaled quantities for a typical Caltech argon $\beta_0 = 10^{-2}$ laboratory plasma and two solar situations, namely, $\beta_0 = 10^{-2}$ corona and $\beta_0 = 10^{-2}$ chromosphere. Table 1 shows that Equations 1a–1d describe the *same* dimensionless space-time evolution for (i) an event lasting 15 μs in a 2 eV argon laboratory plasma having reference density 3×10^{16} cm^{-3} and reference magnetic field 10 kG and (ii) a morphologically similar solar corona event lasting 19 s having $T_0 = 90$ eV, reference density 10^{10} cm^{-3}, and reference magnetic field 40 G. Stating that the reference density is 10^{10} cm^{-3} does not mean that the density has this value at all times or locations but rather means that 10^{10} cm^{-3} is a convenient unit in which to measure density, so the actual density ranges from some fraction of this density (e.g., 1/4) to some multiple of this density (e.g., 4 times). To make the laboratory plasma act as a scale

Table 1
Reference Parameters, Alfvén Velocities, and Times for Scaling Lab Plasma to Solar Corona and Chromosphere

Reference parameter	Symbol (units)	Caltech Lab	Corona	Chromosphere
Mass density	ρ_0 (kg/m^3)	2×10^{-3} Ar	1.7×10^{-11} H	1.7×10^{-9} H
Length	l_0 (m)	0.3	1.6×10^{7}	5×10^{5}
Magnetic field	B_0 (T)	1.0	0.004	0.006
Number density	n_0 (m^{-3})	3×10^{22}	10^{16}	10^{18}
Temperature	T_0 (eV)	2	90	2
Alfvén velocity	v_{A0} (m/s)	2×10^{4}	8.7×10^{5}	1.3×10^{5}
Time	τ_{A0} (s)	1.5×10^{-5}	18	4
Beta	β_0	10^{-2}	10^{-2}	10^{-2}

Note. Lab, corona, and photosphere plasmas are all modeled by Equations 1a–1d, that is, by ideal MHD. Parameters that describe behavior beyond the scope of ideal MHD are given in Table 2 and are discussed in section 4.9.

model of the solar situation, the dimensionless initial and boundary conditions must be the same; a numerical MHD solution of Equations 1a–1d then gives identical results for the laboratory and solar plasmas.

This discussion shows that laboratory experiments can be scaled to the solar corona to the extent that both the experiments and the solar corona are characterized by ideal MHD. However, many phenomena exist beyond the scope of ideal MHD, and these phenomena are in general not directly scalable. Nevertheless, the experiments provide useful insights regarding many of these non-MHD phenomena, and these insights can be applied to the solar corona even if direct scaling is not possible (this will be discussed in sections 4.9 and 4.12).

3. Plan of the Paper, Diagnostics, and Types of Configuration

To keep this paper within length requirements, it will be restricted to a qualitative overview of the main experimental results and their physical interpretation. Reference will be given to the original papers where experimental results and analysis are presented; a detailed and extensive discussion is also available in Bellan (2018c). The experiments used a wide range of diagnostics including high-speed movies of both visible and extreme ultraviolet (EUV) radiation, stereo imaging, three-dimensional volumetric measurement of the time-dependent magnetic field vector, electric current measurement, voltage measurement, X-ray emission, emission of various plasma waves, spectroscopic measurements of density via Stark broadening, temperature and bulk motion via Doppler broadening/shift, magnetic field via Zeeman splitting, density via laser interferometry, and density and electron temperature via Thomson scattering. Two types of geometries have been used; the first will be called bipolar and the second coaxial. The bipolar geometry has the topology of a single coronal loop. The coaxial geometry has eight initial interacting loops similar to the legs of a spider with the eight loops merging to form a coaxial jet. Plasma parameters for both configurations are in the range $n\sim10^{21}$–10^{23} m^{-3}, $B\sim0.05$–0.5 T, $I\sim50$–150 kA, $T\sim2$–3 eV, radius ~2–5 cm, and length ~5–50 cm, and the time interval between shots is 2 min. Shot-to-shot reproducibility is 3–10% depending on operating regime and what is being measured. In the rest of this chapter, the direction *axial* will refer to the direction going from one electrode to the other, and the direction *azimuthal* will refer to the direction of the magnetic field associated with an axial current. There is thus an axial magnetic field and an axial current with the axial current making an azimuthal magnetic field that links the axial magnetic field. This linking corresponds to there being magnetic helicity and to the total magnetic field being twisted or helical.

3.1. Bipolar Geometry and Operation

Figure 1 sketches the basic experimental sequence used to create laboratory plasmas having shape and dynamics similar to solar corona loops (Hansen & Bellan, 2001; Stenson & Bellan, 2008, 2012), while Figure 2 shows the actual electrode configuration and photographs of typical plasmas. First, an electromagnet (Figure 1a) produces an initial quasi-static (5 ms timescale), arch-shaped potential magnetic field with a 10–20 cm characteristic length. The much larger vacuum chamber dimension means that the plasma is unaffected by the vacuum chamber side walls and so behaves as if in semi-infinite space. After the potential magnetic field has been established, high-speed electromagnetically pulsed gas valves briefly puff a neutral gas cloud into the region between the magnet poles. The amount of injected gas is arranged to enable breakdown in the next step of the sequence where a high-energy capacitor bank charged to several kilovolts is connected

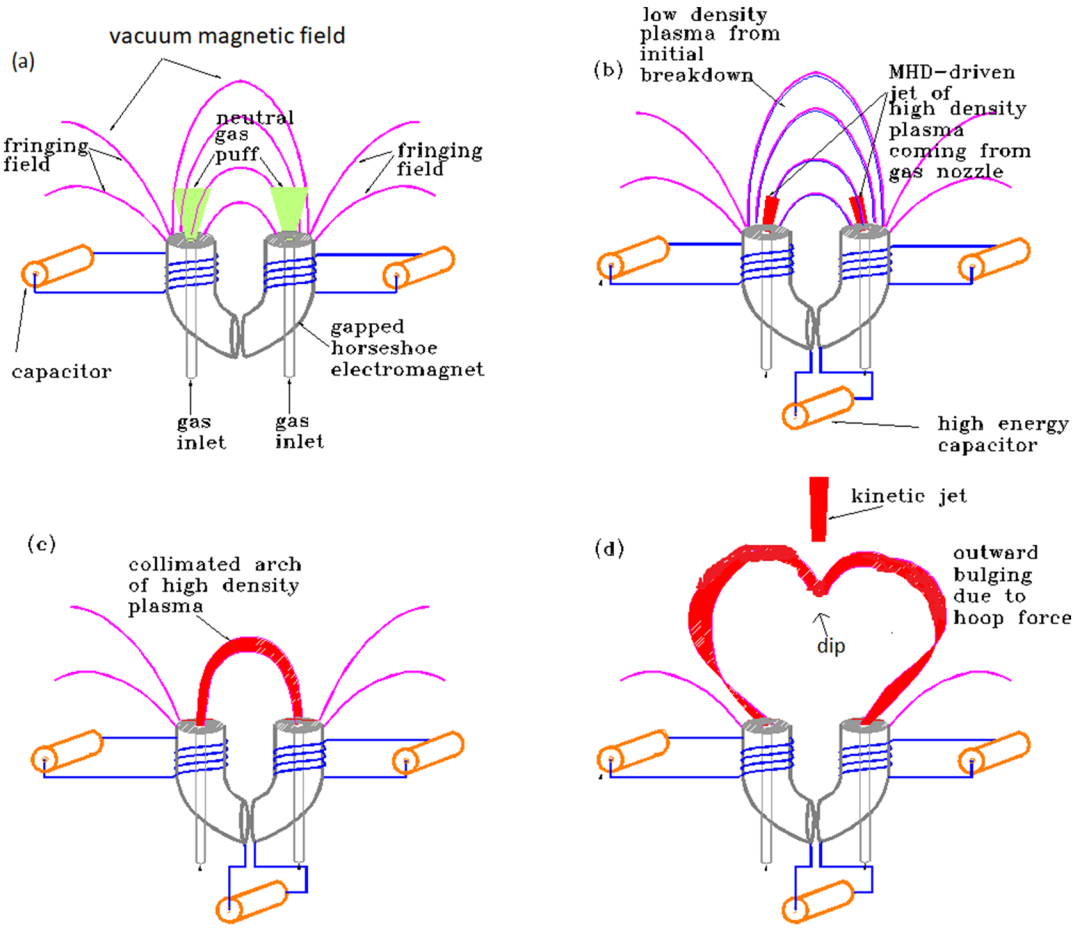

Figure 1. Bipolar source sequence of operation: (a) electromagnets are energized and neutral gas is puffed in; (b) high voltage is applied across electrodes breaking down neutral gas to form weakly ionized plasma, and with increasing axial current MHD forces drive upward plasma jets from both foot points; (c) the plasma flowing up from the foot points forms a dense collimated loop; (d) the loop major radius expands from hoop force with optional dip at apex and optional kinetic jet.

by a high-speed electronic switch across the magnet poles (Figure 1b). The high voltage breaks down the neutral gas in about 0.1 μs to form a low-density plasma (Figure 1b). The electric current flowing through the tenuous plasma produced at breakdown is small and follows the arched vacuum field lines. This current then ramps up and by 5–7 μs has attained several tens of kA. The MHD force associated with this large electric current drives fast upflowing plasma jets from both foot points (Figure 1b). These upflowing plasma jets quickly collide at the apex of the arched loop and fill the flux tube with plasma. The flux tube collimates (Figure 1c) as the two jets collide. All the while, the magnetic hoop force causes an expansion of the arch major radius (Figure 1d). A dip is often observed at the apex and, in certain situations, a kinetic jet appears at the loop apex (Figure 1d).

The sequence shown in Figure 1 occurs only if neutral gas is injected. The jet upflows from the foot points shown in Figure 1b are predicted in Bellan (2003) and have been modeled numerically by Zhai et al. (2014), and recently the force driving these flows has been measured by Haw and Bellan (2017). The jet upflows were demonstrated by Stenson and Bellan (2008, 2012) who injected different gases at the two foot points so that injected gas could be clearly associated with its originating foot point. Blueshifts associated with the upflows have been measured by Tripathi et al. (2007).

3.2. Coaxial Geometry and Operation

The coaxial magnetized plasma source is similar but has coaxial symmetry and consists of a copper disk surrounded by a concentric coplanar copper annulus. The coaxial source has a coil located behind the gap

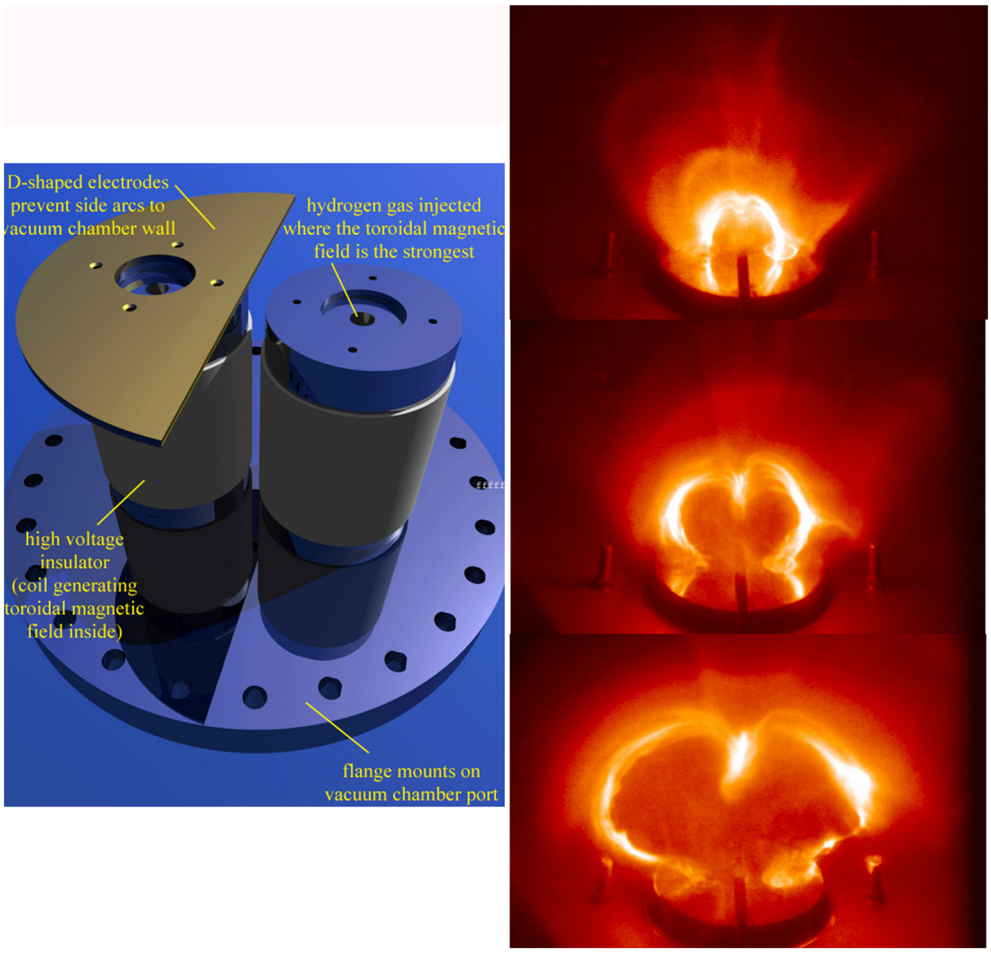

Figure 2. Bipolar configuration. (left) Electrodes (D-shaped electrode used on both sides, but only left side shown here). (right) Time sequence (increasing time going downward) showing hoop force expanding major radius, collimation, and dip at apex (credit for figure on left: Hansen & Bellan, 2001).

between the disk and the annulus; this coil provides a bias poloidal magnetic flux linking the disk to annulus (poloidal refers to the *r*-*z* plane in a cylindrical coordinate system). The sequence of operation is similar to the solar loop plasma and is as follows. First, an external coil is energized to produce a 1–2 mWb poloidal magnetic flux linking the inner copper disk to the outer copper annulus. Next, gas (H, Ar, N, Ne, Kr, or Xe) is puffed through eight orifices on the disk and eight on the annulus. Then a several kilovolt potential drop is applied across the gap separating disk from annulus. The high voltage breaks down the injected gas to form eight arched, plasma-filled flux tubes ("spider legs") linking the disk to the annulus as in the 4 μs image of Figure 3. Each spider leg is similar to a solar loop plasma and electric current driven by the applied voltage flows along each spider leg. Since the spider legs carry parallel currents, their inner segments mutually attract and merge (4.5 to 6 μs in Figure 3) to form a central column jet (6 μs in Figure 3) which lengthens (6.5 to 10 μs) and then becomes kink unstable (10 μs in Figure 3). This merging requires a magnetic reconnection because the merged spider legs wrap around each other, so the magnetic topology has changed from separated distinct spider legs to spider legs wrapped around a common axis. Zhai (2015) imaged this wrapping by injecting nitrogen from Inner Nozzles 1–4 and argon from Inner Nozzles 5–8 and then used filters in front of the camera to distinguish argon from nitrogen. After the spider legs have merged, the lengthening jet behaves in a manner consistent with ideal MHD, that is, consistent with the assumption that the electric field vanishes in the frame moving with the jet. Having $\mathbf{E} = 0$ in the jet frame is an essential property of a numerical simulation of the jet experiment (Zhai et al., 2014) and of an analytic model of the lengthening jet (Bellan, 2020).

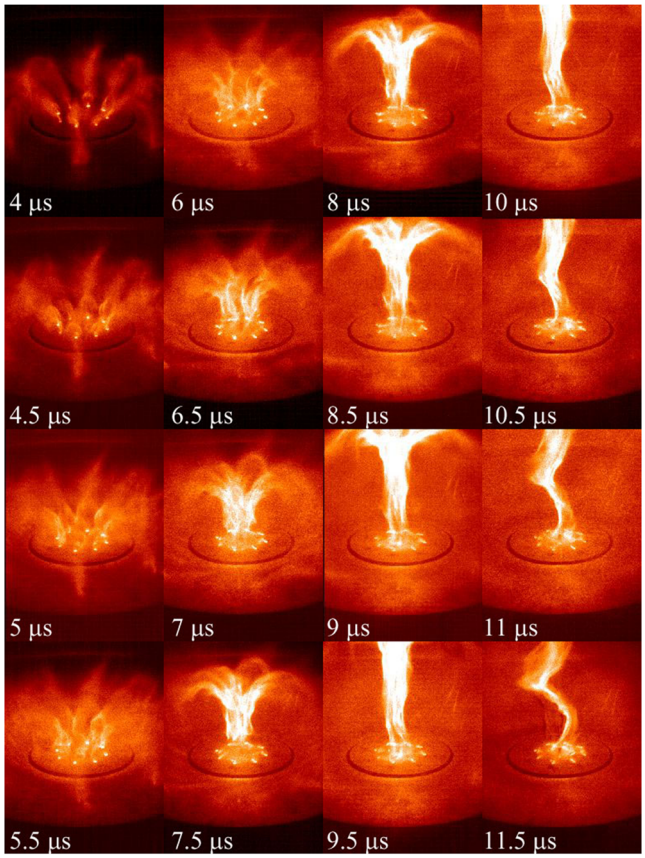

Figure 3. Coaxial sequence: At 4 μs eight spider legs each go from a gas nozzle on the inner 20 cm diameter disk electrode to a gas nozzle on outer annulus electrode. At 5–6.5 μs the inner spider legs merge to form a central column. At 6.5–10 μs the central column lengthens and so constitutes a jet. At 10 μs the jet starts to kink (reprinted figure with permission from You et al., 2005; Copyright 2005 by the American Physical Society).

3.3. Importance and Characterization of the J × B Magnetic Force

The MHD equation of motion, Equation 1a, prescribes the motion of a plasma subjected to the combined $\mathbf{J}\times\mathbf{B}$ and hydrodynamic $-\nabla P$ forces. The MHD induction equation, Equation 1b, simultaneously prescribes the constraint that magnetic flux is frozen into the frame of the moving plasma. The experiments reveal the importance of the current density $\mathbf{J}(\mathbf{x},t)$. Until recently, $\mathbf{J}\times\mathbf{B}$ forces have been generally ignored in solar corona models where attention has instead focused on magnetic field line motion as the prime agent governing solar corona behavior (Parker, 1996, 2007); often the magnetic field is assumed to be potential (i.e., $\mathbf{B}=\nabla\chi$ so $\mathbf{J}=\mu_0^{-1}\nabla\times\mathbf{B}=0$) or force-free so $\mathbf{J}\times\mathbf{B}=0$. However, in a low β plasma such as the solar corona, it is clearly important to understand implications of the $\mathbf{J}\times\mathbf{B}$ force because it is this force that drives the plasma motion. Most obviously, the $\mathbf{J}\times\mathbf{B}$ force is finite only where $\mathbf{J}$ is finite which is the case only when the magnetic field is nonpotential and $\mathbf{J}$ is not parallel to $\mathbf{B}$. On the other hand, $\mathbf{B}$ is finite nearly everywhere as magnetic field nulls are points in three-dimensional space and so have infinitesimal volume (Greene, 1988), that is, are of measure 0. Because forces can exist only if $\mathbf{J}$ is finite, it is reasonable to consider $\mathbf{J}$ to be the prime agent governing dynamical behavior. The special case where $\mathbf{J}$ is finite but parallel to $\mathbf{B}$ so as to give force-free equilibria cannot exist when dynamical behavior (e.g., eruption) occurs because a force is required to accelerate both the plasma and its embedded magnetic field away from equilibrium in order to have dynamics.

Numerous situations have been proposed where the $\mathbf{J}\times\mathbf{B}$ force drives important dynamics (Chen, 2003; Khodachenko et al., 2003; Kliem & Torok, 2006; Melrose, 1995), and these situations cannot be described by potential or force-free models nor by models restricted to describing the motion of magnetic field lines. Controversy has existed regarding whether the electric current and magnetic forces are important. A point of view that the electric current and resulting magnetic forces are neither fundamental nor important has been advocated by Parker (1996, 2001, 2007) who asserted that the magnetic field rather than the electric current is fundamental and objected to the electric current point of view invoked here and previously by Alfvén and Carlqvist (1967), Alfvén (1986), and Melrose (1995). In the author's opinion this dispute is analogous to arguing in mechanics whether acceleration or velocity is the more fundamental quantity, that is, the "prime mover"; arguing that magnetic field is the prime mover is like arguing that velocity is the prime mover driving acceleration. The question of whether current is a cause or an effect was discussed in Bellan (2003) where it was shown that, in the context of a flux rope intercepting a surface with prescribed boundary conditions, the axial component of the current can be considered to be a cause, whereas the azimuthal component of the current can be considered to be an effect. This is because the axial component of the current is determined by the boundary condition imposed at the surface being intercepted (electrode in experiment, solar surface on the Sun), whereas the azimuthal component of the current does not intercept a surface and so is instead determined by the extent to which the axial magnetic field is either compressed or rarefied as a result of the competition between the pinch force, the internal pressure, and the external pressure. In the experiments the axial component of the current comes from electrodes and is dictated by the power supply, while on the Sun the axial component of the current comes from some undetermined source that exists beneath the solar surface. The azimuthal component of the current is a consequence of the axial magnetic field lines being squeezed together by the pinch force associated with the axial current (paramagnetism) or being spread apart as a result of the internal pressure (diamagnetism); this competition between paramagnetism and diamagnetism has been discussed in the tokamak context by Li and Cross (1994). The MHD Ohm's law expressed as $\mathbf{E}+\mathbf{U}\times\mathbf{B}=\eta\mathbf{J}$ is agnostic about the value of current density $\mathbf{J}$ in the limit that $\eta\to 0$, that is, in the ideal limit. Thus, for any given finite current density $\mathbf{J}$, η can be

considered to be so small that $|\eta\mathbf{J}| \ll |\mathbf{E}|$ and $|\eta\mathbf{J}| \ll |\mathbf{U}\times\mathbf{B}|$, so Ohm's law can be considered to be $\mathbf{E}+\mathbf{U}\times\mathbf{B}=0$. However, as will be shown in section 4.9 when the spatial gradient scale becomes so small as to be of the order of the ion skin depth $d_i = c/\omega_{pi}$, Ohm's law is no longer given by ideal MHD and changes to a form that depends on $\mathbf{J}$ via Hall terms.

The $\mathbf{J}\times\mathbf{B}$ force can be characterized in several equivalent ways. These characterizations provide an intuitive sense for how a system will evolve without having to go to the effort of constructing a detailed solution to the nonlinear system of equations. One required feature of any characterization is that it must not imply the existence of a force along the magnetic field since clearly $\mathbf{J}\times\mathbf{B}\cdot\mathbf{B}=0$; thus, the commonly used concept of field line "tension" cannot be correct because a tension would be a force along a field line. Three useful characterizations of the $\mathbf{J}\times\mathbf{B}$ force are provided below and will be referred to in the rest of this chapter. In the author's opinion these are respectively the simplest, the most accurate, and the most profound characterizations.

The *simplest* way to characterize the $\mathbf{J}\times\mathbf{B}$ force is the statement that *parallel currents mutually attract, whereas antiparallel currents mutually repel*. Mutual attraction between parallel currents is the basis of the pinch force that provides confinement of finite pressure plasmas. Mutual repulsion between antiparallel currents provides the hoop force that drives the kink instability (Hsu & Bellan, 2003), the expansion of the major radius of an arched flux rope (Chen et al., 2006; Stenson & Bellan, 2012), the torus instability (Kliem & Torok, 2006), and magnetically driven jets (Bellan, 2018a, 2018b; Kumar & Bellan, 2009).

The *most accurate* way of characterizing the magnetic force is to use the vector identity $\nabla B^2/2 = \mathbf{B}\cdot\nabla\mathbf{B} + \mathbf{B}\times\nabla\times\mathbf{B}$ together with Ampere's law $\nabla\times\mathbf{B}=\mu_0\mathbf{J}$ to express the magnetic force as

$$\begin{aligned}\mathbf{J}\times\mathbf{B} &= \frac{1}{\mu_0}(\nabla\times\mathbf{B})\times\mathbf{B}\\ &= -\nabla\left(\frac{B^2}{2\mu_0}\right)+\frac{1}{\mu_0}B\hat{B}\cdot\nabla\left(B\hat{B}\right)\\ &= -\nabla\left(\frac{B^2}{2\mu_0}\right)+\frac{1}{\mu_0}\left(B\hat{B}\cdot\nabla B\right)\hat{B}+\frac{1}{\mu_0}B^2\hat{B}\cdot\nabla\hat{B}\end{aligned} \tag{4}$$

so

$$\boldsymbol{J}\times\boldsymbol{B} = -\nabla_\perp\frac{B^2}{2\mu_0}+\frac{1}{\mu_0}\kappa B^2. \tag{5}$$

Here

$$\nabla_\perp = \nabla-\hat{B}\left(\hat{B}\cdot\nabla\right) \tag{6}$$

is the gradient in the direction perpendicular to the magnetic field and

$$\kappa = \hat{B}\cdot\nabla\hat{B} = -\frac{\hat{R}}{R} \tag{7}$$

characterizes field curvature where R is the local radius of curvature of the magnetic field and $\hat{R}$ is a unit vector pointing out from the center of curvature along the radius of curvature.

The first term on the right-hand side (RHS) of Equation 5 (i.e., term involving $\nabla_\perp$) is called the magnetic pressure term; the second term (term involving $\boldsymbol{\kappa}$) is called the magnetic curvature term. Both these terms are perpendicular to $\mathbf{B}$, so both provide no forces along the magnetic field (to see that the curvature term is perpendicular note that $\frac{1}{2}\nabla\left(\hat{B}\cdot\hat{B}\right)=0=\hat{B}\cdot\nabla\hat{B}+\hat{B}\times\nabla\times\hat{B}$). If the magnetic field is potential (i.e., $\mathbf{J}=0$) then the left-hand side (LHS) of Equation 5 vanishes, so the two RHS terms must be equal in magnitude and opposite in sign showing that it can be dangerous and misleading to try to explain magnetic forces using just one of these RHS terms. If the magnetic field is force-free (i.e., $\mathbf{J}$ is finite, but parallel to $\mathbf{B}$) the two terms on the RHS of Equation 5 again cancel. Finally, there is the possibility that one or the other of the two terms on the RHS of Equation 5 dominates. If the magnetic pressure term dominates, then the magnetic pressure force pushes plasma from regions of large magnetic field to regions of small magnetic field, but only in a direction perpendicular to the magnetic field. If

the magnetic curvature term dominates, then the magnetic force pushes the plasma in a direction required to straighten out the curvature. This straightening of curvature is analogous to the consequence of a tension force on a plucked guitar string, so the effect of the curvature force is partially like the effect of a tension force. However, in contrast to guitar string tension, the magnetic curvature force only acts to straighten out magnetic field curvature and does not act to contract the length of a magnetic field line (i.e., there is no force parallel to **B**).

The balance between magnetic curvature and magnetic pressure forces can be intricate. An important example is the situation of a uniform, finite-radius axial current I as in a wire. If the current radius is given by a so $J_z = I/(\pi a^2)$ for $r < a$ and $J_z = 0$ for $r > a$, then from Ampere's law the associated azimuthal magnetic field is $B_\phi = \mu_0 I r/(2\pi a^2)$ for $r < a$ and $B_\phi = \mu_0 I/(2\pi r)$ for $r > a$. For $r < a$, the magnetic pressure force is thus $-(2\mu_0)^{-1}\nabla_\perp B^2 = -I^2 r\hat{r}/\left(4\pi^2\mu_0 a^4\right)$, while the magnetic curvature force is $\kappa B^2/\mu_0 = -I^2 r\hat{r}/\left(4\pi^2\mu_0 a^4\right)$, so here the magnetic pressure and magnetic curvature forces are identical and add to give a net inward force $\mathbf{J}\times\mathbf{B} = -I^2 r\hat{r}/\left(2\pi^2\mu_0 a^4\right)$. This is the pinch force that in equilibrium balances an outward force due to $-\nabla_\perp P$ and so provides plasma confinement. However, for $r > a$, the magnetic pressure force is $-(2\mu_0)^{-1}\nabla_\perp B^2 = I^2\hat{r}/\left(4\pi^2\mu_0 r^3\right)$, while the magnetic curvature force is $\kappa B^2/\mu_0 = -I^2\hat{r}/\left(4\pi^2\mu_0 r^3\right)$, so the magnetic pressure and magnetic curvature forces, being equal and opposite, cancel to give no net force. The magnetic pressure force is closely related to the mutual repulsion between antiparallel currents since a magnetic field maximum exists between antiparallel currents; an example is the "hoop force" where oppositely directed currents on the opposite sides of a current loop mutually repel and act to increase the loop major radius.

The *most profound* way of characterizing the MHD force is based on consideration of the energy stored in the entire volume V of magnetic field for given, fixed boundary conditions. This consideration is based on a variational argument (see pp. 306–309 of Bellan, 2006) which shows that of all the possible magnetic fields satisfying a given boundary condition, the potential field is the one having the lowest total magnetic energy $W = (2\mu_0)^{-1}\int_V B^2 d^3 r$. Furthermore, this consideration shows that force-free fields are local minima of W. This is analogous to the energy structure of an atom where the potential magnetic field corresponds to the ground state and force-free magnetic fields correspond to higher-energy stable quantum states. An arched flux rope is nonpotential to the extent that it is twisted since twist corresponds to the existence of current. A large axial current will give a large upward $\nabla_\perp B^2$ force which is in the direction to cause eruption since the magnetic field is stronger on the concave side of the arch than on the convex side (e.g., consider electric current flowing from the left foot point to the right foot point in Figure 1 and in the photos in Figure 2). However, the force associated with curvature of the axial magnetic field opposes eruption, so the axial electric current has to be sufficiently large for its upward $\nabla_\perp B^2$ force to overwhelm the downward directed magnetic curvature force associated with the axial magnetic field. The situation is analogous to blowing up a balloon where the magnetic pressure force corresponds to the pressure in the balloon trying to make the balloon radius larger and the magnetic curvature force corresponds to the stretching of the balloon skin which is trying to make the balloon radius smaller.

The induction equation Equation 1b has the property of freezing magnetic flux into the frame of the moving plasma (see derivation on pp. 56–57 of Bellan, 2006). This means that one can draw an arbitrary closed contour C in three-dimensional space and define S as the surface for which this contour is a perimeter, and then the flux $\int_C \mathbf{B}\cdot\mathbf{ds}$ will remain the same if the contour moves with the plasma. Since the contour is arbitrary, this means that one could draw a first contour in one plane (e.g., the xy plane) and another contour in an orthogonal plane (e.g., the yz plane) and the two separate fluxes respectively linked by each of these initially orthogonal contours would remain constant as the contours deform because of plasma motion.

4. Discussion of the Experiments and Their Main Results

4.1. Flux Rope Self-Collimation and Associated Axial Flows

Collimation, that is, uniform cross section along the length, is a striking feature of both actual solar corona loops and the scaled-down replicas produced in the Caltech laboratory experiments. This filamentary structure is counter to what was expected by solar observers (e.g., see Klimchuk, 2000) because it was presumed that the axial magnetic field of a loop would weaken with increasing distance from the solar surface. Since

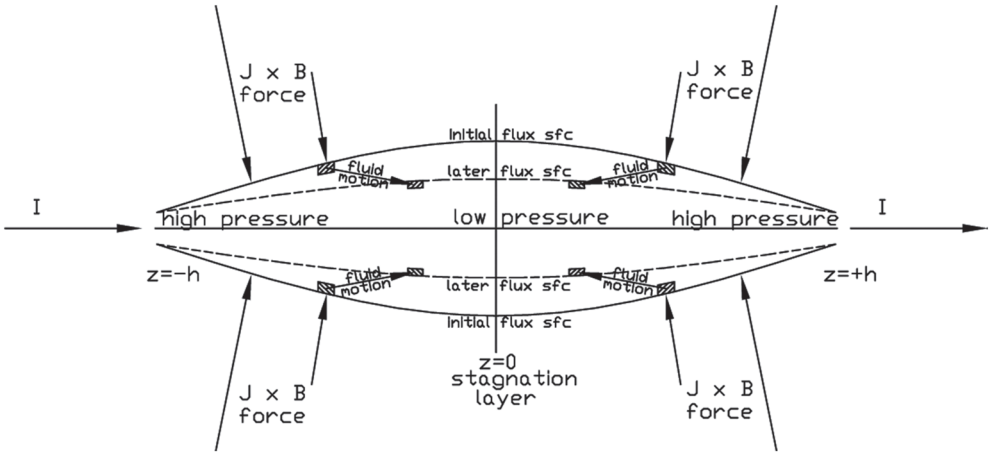

Figure 4. MHD-driven flows go from both foot points to middle (apex) and pile up both plasma and embedded azimuthal flux, resulting in pinching and increased density (reproduced from Bellan, 2003, with the permission of AIP Publishing).

the flux BA is constant along a flux tube, weaker B should mean larger cross-sectional area A. The observed near-uniformity of A along the flux tube indicates that the axial field B is nearly constant along the length of the flux tube and is not getting weaker as was expected.

Collimation is observed in the single coronal loop (see Figure 2, right), in the spider legs (see Figure 3), and in the jet plasma resulting from the merging of the spider legs in Figure 3. These observations motivated a model to explain collimation (Bellan, 2003). This model shows that when electric current is made to flow along an uncollimated magnetic flux tube, MHD forces drive axial plasma flows from the thin (small cross section) to fat (large cross section) parts of the flux tube. In the case of coronal loops this thin to fat motion corresponds to driving flows from both foot points toward the apex. On the flux tube axis these forces are in the form of axial pressure gradients because there can be no magnetic force along the axis, while off axis the forces are the axial component of the $\mathbf{J}\times\mathbf{B}$ force. Axial pressure gradients exist on the axis because the radial pinch force is stronger where the flux tube radius a is small than where a is large since for a given total axial current the pinch force scales as a^{-4} as discussed in section 3.3. Radial pressure balance then results in a larger on-axis pressure where a is small (i.e., foot points) than where a is large (i.e., apex). As sketched in Figure 4 which is a straightened-out version of an arched flux tube, these axial flows carry frozen-in azimuthal magnetic flux from the foot points to the apex (at $z=0$ in Figure 4) where the convected azimuthal magnetic flux and the flowing plasma accumulate. However, accumulation of azimuthal magnetic flux means that the azimuthal magnetic flux density is increasing and since magnetic field strength is the same as flux density, the azimuthal magnetic field B_ϕ increases. The pinch force associated with the increased B_ϕ squeezes down the radius of the fat midsection of the flux tube and so causes the flux tube to become collimated. Collimation is thus associated with flows from both foot points filling the flux rope up with plasma (see Figures 1b and 1c); this was called the "gobble" model because it appears as if the initial arched flux rope ingests plasma at its foot points. The gobble effect can also be seen from examination of the induction equation (Bellan et al., 2005) which can be configured for a straight axis flux rope to show that $B_\phi/\rho r$ is invariant at the axial midpoint where the opposing flows collide ($z=0$ plane in Figure 4). This means that increasing ρ at $z=0$ and at some given radius r as a result of inflowing plasma necessarily increases B_ϕ and so causes pinching; the radius a has to decrease to maintain $2\pi aB_\phi=\mu_0 I$ where I is the axial current flowing from left to right in Figure 4. At the stagnation layer where the flows from the left and from the right collide ($z=0$ layer in Figure 4) there cannot be a directed flow, and so the kinetic energy of flow must be converted into heat via collisions; this is somewhat of an oversimplification because the counterstreaming flows will in reality flow through each other for some distance and then dissipate because of collisions between the counterstreaming motions. Thus, the stagnation of the flows heats the plasma. The gobble model thus provides a self-consistent and testable hypothesis for why magnetic flux tubes having an axial electric current are bright, hot, plasma-filled, and collimated. Experiments testing the gobble model have supported this model. For example, the MHD $\mathbf{J}\times\mathbf{B}$ axial forces predicted by the gobble model have been directly observed by Haw

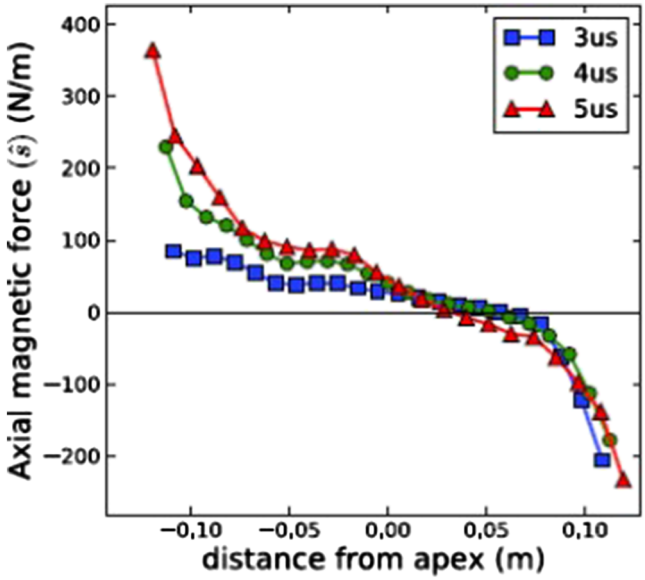

Figure 5. Measured axial component of $\mathbf{J}\times\mathbf{B}$ force as a function of distance from apex. This corresponds to the horizontal component of the $\mathbf{J}\times\mathbf{B}$ arrows in Figure 4 (reprinted figure with permission from Haw & Bellan, 2017; Copyright 2017 by John Wiley and Sons).

and Bellan (2017) using an array of magnetic probes that measured the time-dependent vector magnetic field over a large volume. The current density $\mathbf{J}$ was determined using $\mathbf{J}=\mu_0^{-1}\nabla\times\mathbf{B}$ and, then the component of $\mathbf{J}\times\mathbf{B}$ parallel to the flux rope axis was seen to be such as to drive flows from both ends (foot points) of the flux rope toward the middle (apex). This measurement showing magnetic forces driving flows from both ends toward the middle is shown in Figure 5. Single-ended flows such as in Figure 3 are similarly collimated as discussed in Bellan (2018a, 2018b, 2018c). MHD-driven flows have also been discussed by Shibata and Uchida (1986).

The gobble model prediction of upflows from both foot points should be observable as Doppler blueshifts for an observer looking toward the foot points. These blueshifts at both foot points of the laboratory replica of a solar corona loop have been observed by Tripathi et al. (2007), and these observations are shown in Figure 6. Spectroscopic measurements of Doppler shifts of emission lines from hot ions in the upper transition region and corona at the center of the solar disk made by Peter and Judge (1999) using the SUMER instrument on the SOHO spacecraft have also indicated blueshifts with an average value corresponding to upflows of the order of 5 km/s. The solar blueshifts reported by Peter and Judge (1999) are thus consistent with the gobble model prediction of upflows from foot points of solar corona loops and would be the result of averaging over a multitude of solar loops.

Stenson and Bellan (2008) vividly demonstrated the flows originating from the foot points using a scheme where different gases were injected at the two foot points. Stenson and Bellan (2008) generated Figure 7 by putting atomic line filters in front of the camera to distinguish the two gases from each other. The composite red/purple color-coded image in Figure 7 was then constructed from two camera images using a computer. Because the red gas (hydrogen) in Figure 7 is lighter than the purple gas (nitrogen), the red gas goes faster and further and thus fills up a larger fraction of the flux tube. This figure also shows that the flux tube major radius increases as the lengths of the two jets increase. The flow velocity, being driven by magnetic forces, greatly exceeds thermal velocities (Kumar & Bellan, 2009; Stenson & Bellan, 2012); this is consistent with having $\beta\ll 1$. Plasma density in the arched loop results from the plasma ingested by the jet upflow; this

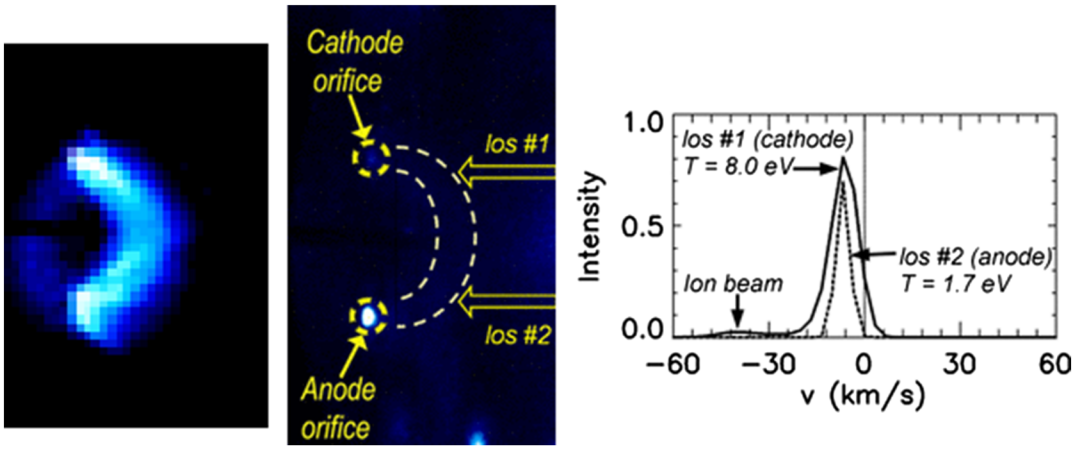

Figure 6. (left) Photo of experimental replica of solar corona loop at $t=1\,\mu$s after breakdown. (middle) Sketch showing lines of sight (LOS #1 and #2) of fiber optic with collimator that goes to spectrometer for measurement at this time. (right) Measured spectra for LOS #1 and LOS#2; coordinate system defined relative to observer, so negative velocity is motion toward observer (blue-shifted as seen by observer). This figure uses material excerpted with permission from Figures 1, 4, and 5a in Tripathi et al. (2007). Copyright 2007 by the American Physical Society.

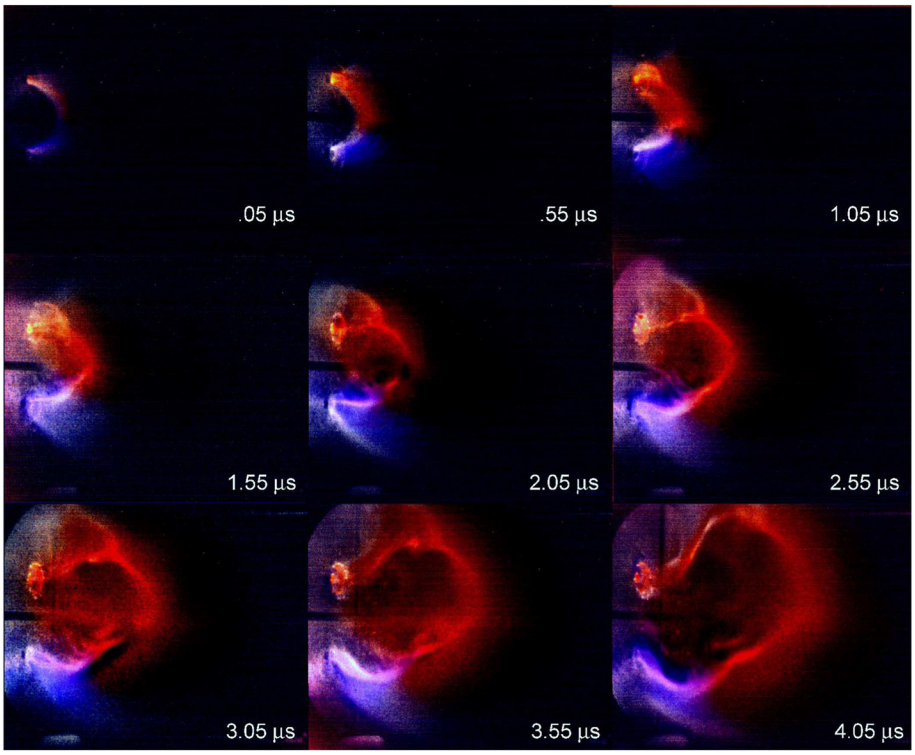

Figure 7. Demonstration that gas in loop originates from the foot points. Hydrogen (red) is injected from top foot point, and nitrogen (purple) is injected from bottom foot point. The loop consists of a lengthening hydrogen jet butting against a lengthening nitrogen jet. The hydrogen jet is longer because hydrogen, being lighter, is accelerated to higher velocity. The arch major radius increases because of the hoop force (stronger azimuthal magnetic field on concave side than on convex side of arch). ©2008 IEEE. Reprinted, with permission, from Stenson and Bellan (2008).

density is orders of magnitude larger than the density of the neutral gas initially puffed in to enable breakdown (You et al., 2005). The magnetic configuration thus depends on the mass flux boundary condition as well as on the magnetic and electric current boundary conditions.

4.2. Eruptions

The gobble model addressed flows along the axis of a flux tube having a straight axis, an initially axially nonuniform cross section, and an axial current. The gobble model showed that the axial flows would tend to fill the flux tube with plasma and collimate the flux tube. The gobble model did not take into account the curvature of the flux tube axis, that is, the arch-shape of a solar loop. This curvature of the axis, introduces a more global effect wherein current flowing along a curved axis produces forces that tend to increase the radius of curvature. Since the effect of pressure gradients along the axis have already been taken into account in the gobble model, the analysis of the force resulting from the curvature of the current to lowest order involves magnetic forces only.

A solar loop can be considered a half toroid, and so the axial current flowing from one foot point to the other will produce hoop forces (magnetic pressure) that tend to increase the major radius of the half toroid. These currents have to be sufficiently strong to overcome the magnetic curvature force which is directed so as to oppose increase of the major radius. The competition between magnetic pressure and magnetic curvature forces is like having to blow hard enough to inflate a balloon where blowing corresponds to the hoop (magnetic pressure) force and the restraining force of the stretched balloon material corresponds to the magnetic curvature force.

The hoop force on a torus can be quantified by consideration of a virtual displacement of the major radius R of a flux-conserving toroid having minor radius a and toroidal current I. A flux-conserving reduction of the system magnetic energy can be accomplished by the torus increasing its inductance since in electric circuit

terms magnetic energy W can be expressed as $W = LI^2/2 = \Phi^2/2L$ where L is the toroid inductance and $\Phi = LI$ is the magnetic flux linked by the toroid. Since L is approximately proportional to the major radius, a flux-conserving increase of L reduces W. A more exact analysis based on the classic tokamak calculation by Shafranov (1966) is given in Stenson and Bellan (2012) where it is shown that the rate of change of the major radius R as a result of this force can be expressed as

$$\frac{d^2R}{dt^2} = \frac{\alpha}{4\pi^2}\frac{\mu_0}{\rho a^2}\frac{I(t)^2}{R(t)} \tag{8}$$

where $\alpha = \ln(R/a) + 1.08 + l_i/2$, l_i is the torus internal inductance, and ρ is the mass density. Equation 8 is a low β form of Equation 1a and has an exact analytic solution if the current can be approximated as rising linearly with time; that is, if the current can be expressed as

$$I(t) = I_0 t/\tau. \tag{9}$$

This exact solution is obtained by substituting Equation 9 into Equation 8 to obtain

$$R(t) = \frac{1}{2\pi}\sqrt{\frac{\mu_0\alpha}{2\rho}}\frac{I_0}{a\tau}t^2 \tag{10}$$

which is consistent with the experimentally observed dependence $R \sim t^2$ when $I \sim t$ as presented in Stenson and Bellan (2012).

4.3. Merging of Coronal Loops Having Same-Sign or Opposite-Sign Magnetic Helicity

Magnetic helicity is an important parameter characterizing magnetized plasmas because consideration of magnetic helicity provides insights regarding how a system tends to evolve. Magnetic helicity has a precise mathematical definition and can be interpreted intuitively in various equivalent ways: for example, it can be thought of as a measure of the linkage of flux tubes with each other or as the twist of a flux rope. Magnetic helicity has many properties relevant to laboratory experiments and solar corona structures. Only a brief summary of the main features of magnetic helicity will be given here as magnetic helicity has been discussed extensively in the literature (Bellan, 2006, 2018c; Berger & Field, 1984; Calugareanu, 1959; Finn & Antonsen, 1985; Jensen & Chu, 1984; Moffat, 1978; Pfister & Gekelman, 1991; Woltjer, 1958).

The appropriate definition of magnetic helicity depends on whether the system under consideration is isolated or not. If the system is isolated, that is if no magnetic field lines exit the volume under consideration, then the magnetic helicity is simply $K = \int \mathbf{A}\cdot\mathbf{B}d^3\mathbf{r}$ and because no field lines exit the volume this definition is gauge independent. However, when field lines exit the volume under consideration, a considerably more complicated definition, called relative helicity must be used. The definition of relative helicity has the property of counting only those linkages existing within the volume under consideration while excluding all linkages that occur outside this volume. Because magnetic helicity characterizes general topological properties of a system rather than specific geometric details, it conceptually unifies a great range of phenomena that otherwise would seem unrelated. Injecting electric current to flow between two electrodes linked by an initially potential magnetic flux as in Figure 1 corresponds to injecting helicity into a nonisolated system. Similarly, the situation shown in Figure 3, which has a considerably different geometry, also corresponds to injecting helicity into a nonisolated system.

Using the helicity concept identifies several important properties of a magnetized plasma (proofs given in the literature cited above):

1. Magnetic helicity has a sign such that a system with right-handed twist has positive helicity and a system with left-handed twist has negative helicity. Positive helicity corresponds to having an axial current that is parallel to the axial magnetic field; negative helicity has a current that is antiparallel.
2. When magnetic reconnection occurs in an isolated system, magnetic helicity is nearly conserved, whereas magnetic energy is dissipated. This means that after many reconnections the system evolves to a lowest energy state while retaining almost all its original helicity. This final minimum-energy, helicity-conserving state is called a Taylor state and the process of attaining this state is called Taylor

relaxation. The Taylor relaxation analysis ignores dynamics because it assumes that the system slowly evolves through a sequence of equilibria with progressively lower magnetic energies until the minimum-energy state is reached. The experiments described here were initially assumed to be describable by a Taylor relaxation process, but it was then discovered that there is no slow evolution through a sequence of equilibria because the system is highly dynamic. Also, the Taylor state ignores pressure gradients and focusses exclusively on the magnetic field, whereas the systems discussed here are defined by the existence of bright regions (localized high pressure) that clearly show the magnetic field topology. Thus, the Taylor relaxation concept can be considered a useful starting point but not a complete description. The Taylor model describes the magnetic field and omits description of what the plasma is doing (e.g., has localized pressure, has flows, tends to self-collimate).

3. Mathematically, the Taylor state is a zero-pressure, force-free equilibrium governed by the relation $\nabla \times \mathbf{B} = \lambda \mathbf{B}$ where the parameter λ can be interpreted in a number of equivalent ways: (i) λ is an eigenvalue, (ii) λ is the ratio of axial magnetic current to axial magnetic flux, (iii) λ is the ratio of magnetic energy to magnetic helicity in an isolated system, (iv) λ is a measure of the twist, and (v) λ is of the order of the inverse of the characteristic scale length of the system. Because helicity is conserved better than energy, combination of Interpretations (iii) and (v) in this list shows that, if allowed, an isolated system will tend to expand in size because expansion provides a helicity-conserving decrease in stored magnetic energy.
4. When the system is not isolated as is the case in the experiments and in the solar corona, properties of magnetic helicity also depend on the timescale under consideration. On long timescales, substantial helicity might be injected into the system, so the helicity is not conserved (e.g., the lengthening jet in Figure 3), but on very short timescales where negligible helicity is being injected, the system can be considered helicity-conserving (e.g., timescale of kink instability in Figure 3).

An experimental configuration having two adjacent solar corona loops was investigated by Hansen et al. (2004). The configuration was such that the axial electric current was the same for the two loops but the directions of the respective axial magnetic fields could be the same or opposite. In the former case, the two loops have same-sign magnetic helicity, while in the latter case, the two loops have opposite-sign magnetic helicity. Two loops with the same sign corresponds to both loops having right-handed twist or both loops having left-handed twist; two loops with opposite-sign helicity corresponds to one loop having right-handed twist and the other left-handed twist.

Because of the attraction of the same-sense axial electric currents in the two loops, in both the same- and the opposite-helicity cases here the two loops attract each other and merge. However, the behavior of the merged loops is quite different. When loops having the same sign of helicity merge (cohelicity merging), it is observed that the resulting single loop expands at a similar rate to that of a single loop but when loops with opposite-sign helicity merge (counterhelicity merging) the expansion is faster. Also, when counterhelicity loops merge there are substantial bursts of EUV radiation but not for cohelicity merging.

The interpretation for these differing behaviors is that loop expansion involves a competition between the magnetic pressure force ($\nabla_\perp B^2$ force) which is directed to expand the loop major radius and the magnetic curvature force ($\boldsymbol{\kappa}\, B^2$) associated with stretching the axial magnetic field away from its initial vacuum-like configuration. Merging counterhelicity loops reduces the restraining magnetic curvature force while enhancing the expansive magnetic pressure force so as to cause faster expansion. Merging cohelicity loops retains both the restraining magnetic curvature force and the magnetic pressure force, so the expansion rate stays about the same as for a single loop. Since the axial field is much larger than the azimuthal field in a weakly twisted loop, annihilation of the axial field as occurs in counterhelicity merging releases more magnetic energy than happens in cohelicity merging where it is the weaker, azimuthal field that is annihilated. This annihilation of a stronger magnetic field in the counterhelicity merging provides more energyfor electron acceleration and explains why there are strong EUV bursts in the counterhelicity merging case but not in the cohelicity merging case.

Merging of coronal loops necessarily involves magnetic reconnection and dissipation. Dissipation is required because in order for reconnection to be a spontaneous process, it must involve a reduction of the potential energy stored in the configuration in analogy to a ball falling from the top of a hill to a valley being a spontaneous process but not the reverse process. Since in a low β plasma the main form of stored energy is the magnetic field energy, reconnection must involve the system changing to a state of lower magnetic

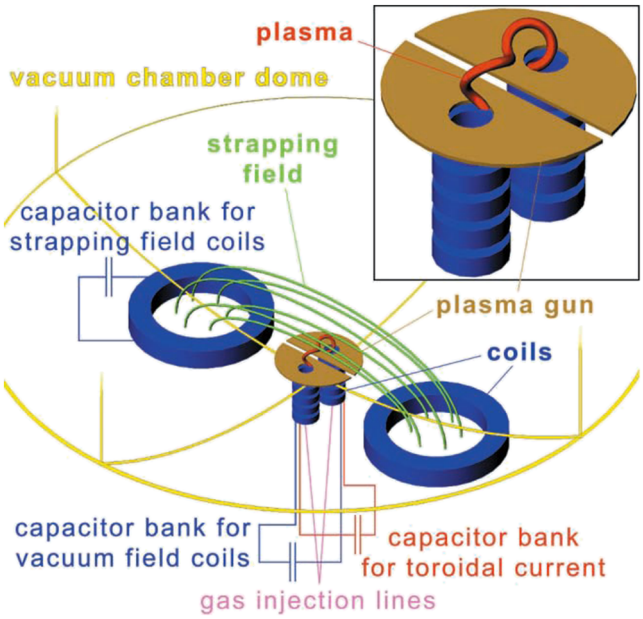

Figure 8. Sketch showing strapping magnetic field (green) produced by external coils (blue) (figure credit: Hansen & Bellan, 2001).

energy. This reduction in energy is accounted for by transformation of the removed magnetic energy into some combination of heat, energetic particles, or waves. Reconnection is required because the topology of the merged loops differs from that of the initial loops. Consider the merging of two identical simple flux loops each with axial flux Φ_0, azimuthal flux ψ_0, axial length L, and axial cross section A. According to the relation between linked flux and helicity, each flux loop initially has a helicity $K = 2\Phi_0\psi_0$, so the initial helicity of the two flux loops is $K_{tot} = 2K = 4\Phi_0\psi_0$. In order to keep K_{tot} constant, the merged structure will have axial flux $\Phi_1 = \sqrt{2}\Phi_0$ and $\psi_1 = \sqrt{2}\psi_0$. There will have to be electric fields associated with this change in helicity-conserving change in flux and these electric fields will drive currents which produce the differential magnetic field that changes the topology, accelerate some particles to high energy, and act as the source for radiation of waves. These processes are not described by Equation 1 but will be considered in section 4.9 where the effects of including resistive, Hall, and electron inertia terms in the generalized Ohm's law will be addressed.

4.4. Strapping Field and the Torus Instability

The hoop force can be opposed not only by the curvature force but also by imposition of an extra magnetic field produced by external coils. This additional magnetic field is arranged to be normal to the plane of the axis of the arched loop as sketched in Figure 8. If the loop is considered to be a half toroid and a cylindrical coordinate system$\{R, \phi, z\}$ is used so that the current along the loop axis is in the ϕ direction, then an external magnetic field in the z direction will produce a force $J_\phi\hat{\phi} \times B_z\hat{z} = J_\phi B_z\hat{R}$. This external field B_z, called the strapping field, opposes the hoop force if the sign of the strapping field is such that $J_\phi B_z$ is negative. An experiment with an externally produced strapping field by Hansen and Bellan (2001) showed that a sufficiently strong strapping field inhibits the eruption as predicted; this is shown in Figure 9.

The torus instability was proposed by Kliem and Torok (2006) and involves a strapping field that decays with altitude at a specific rate (decay index). At low altitude the strapping field is sufficiently strong to oppose the hoop force but at high altitude the strapping field weakens and becomes incapable of opposing the hoop force. If the strapping field increases with altitude up to some critical altitude, but thereafter decreases with altitude, a loop at low altitude will be stable with respect to slight increases in axial current. This is because a

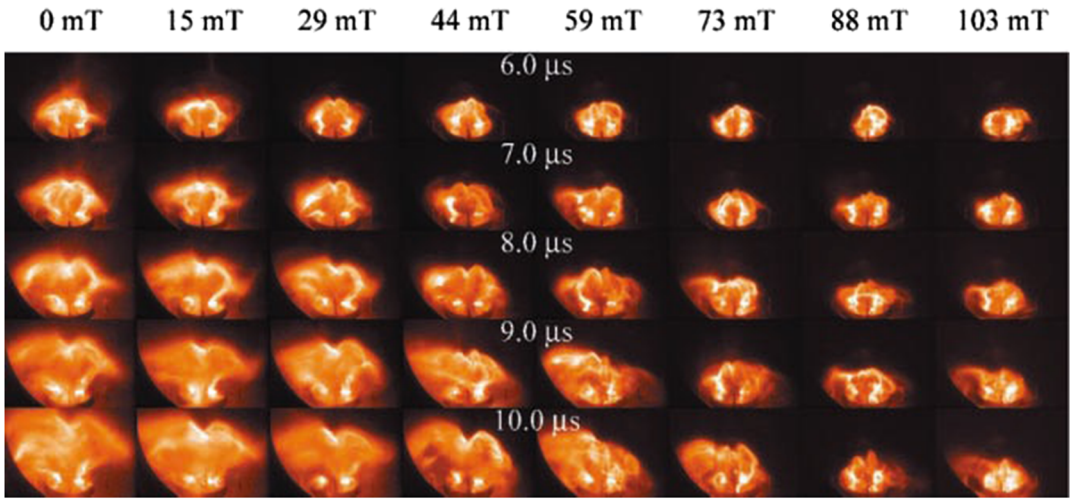

Figure 9. Loop expansion versus time for strapping fields ranging from 0 to 103 mT (figure credit: Hansen & Bellan, 2001).

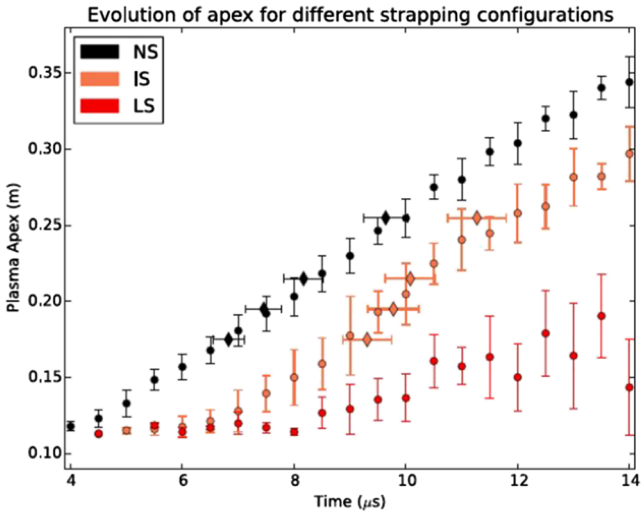

Figure 10. With no strapping field (NS) the increase in height of the loop apex is uninhibited. With a large strapping field (LS) the loop is inhibited from expanding. With an intermediate strapping field (IS) the loop is held down at first, but then at about 6.5 μs escapes and accelerates as in the no strapping field case (reprinted figure with permission from Ha & Bellan, 2016; Copyright 2016 by John Wiley and Sons).

slight increase in axial current will give a slight increase in hoop force which will push the arched loop up slightly higher until its apex reaches an altitude at which the strapping force becomes sufficiently strong to balance the hoop force. However, if the loop is above the critical altitude, a slight increase in current will again give a slight increase in hoop force but now there will be a loss of equilibrium because at higher altitude the strapping field is weaker and so cannot balance the increased hoop force. This loss of equilibrium results in an uninhibited upward expansion, that is, an eruption. Ha and Bellan (2016) set up an experimental situation where a strapping field with a suitably short spatial decay length was produced by coils inside the vacuum chamber and observed that an erupting plasma loop accelerated when it penetrated this region of rapidly decaying strapping field. This experimentally observed initial inhibition of expansion followed by a fast expansion is shown by the IS data in Figure 10. This localized acceleration when the loop apex attains the altitude where the strapping field decays is similar to that observed in numerical models, such as Figure 9 in Fan (2017).

4.5. Apex Dips

A distinct dip at the apex of the laboratory experiment replicas of solar coronal loops is typically observed (see example in Figure 2, right). For many years this dip was presumed to be the projection of a kink but recently Wongwaitayakornkul et al. (2017) determined that the dip occurs because there is higher mass density at the apex than elsewhere on the loop. The reason for this higher density is understood by consideration of the neutral gas jets sketched in green in Figure 1a. Two possible situations can occur just before breakdown depending on the magnitude of the neutral gas collision mean free path compared to the characteristic dimension of the loop apex region. These are (i) at the apex the injected neutral gas mean free path is very large so that the left and right neutral gas jets pass right through each other in which case the neutral gas density at the apex is just the linear sum of the right and left densities, and (ii) at the apex the neutral gas jets are so dense that the neutral gas collision mean free path is very small, so the left and right jets collide resulting in a strong peaking of gas density at the apex in which case the apex gas density greatly exceeds the linear sum of the right and left densities. When ionization occurs in Case (ii), the apex will have a much greater plasma mass density ρ than at loop locations away from the apex and so using Equation 8 it is seen that d^2R/dt^2 will be smaller at the apex than at other locations because ρ is larger at the apex. This greatly reduced acceleration of the apex compared to elsewhere on the loop means that the apex will lag behind and this lag (reduced increase of major radius with time) appears as a dip at the apex.

This interpretation was confirmed by adjusting the amount of injected gas so as to be in Case (i) or (ii). For low injected gas density there is minimal dip as shown in Figure 11a, while for high injected gas density there is a pronounced dip as shown in Figure 11b. Furthermore, by adjusting the relative timing of the left and right foot point gas valves it was possible to move the region of high density to the left or right of center. As shown for the red and cyan cases in Figure 12, the location of the dip moved off center and was located where the mass density was highest. Finally, an erupting loop with higher density at the apex was simulated using a 3-D numerical MHD code. The numerical simulation shows an apex dip essentially identical to that observed experimentally as can be seen by comparing the experimental image in Figure 13a with the synthetic image created from the numerical simulation shown in Figure 13b. This understanding of the apex dip has important implications for the solar context because it shows that the acceleration of each segment of a flux rope is inversely related to the mass density in the specific segment, that is, it reveals the importance of mass loading, a dependence missing from both potential and force-free field models of the solar corona. This may be relevant to the static equilibrium of prominences where dips are observed to occur at regions of high localized density (Su & van Ballegooijen, 2012). In the prominence situation, static upward $\mathbf{J}\times\mathbf{B}$ forces compete with the downward solar gravity, so in locations of greater local mass density, the gravitational force is locally greater resulting in a dip. The lab experiment has no gravity and instead dynamic $\mathbf{J}\times\mathbf{B}$ forces accelerate the loop major radius and where the material being accelerated is locally more

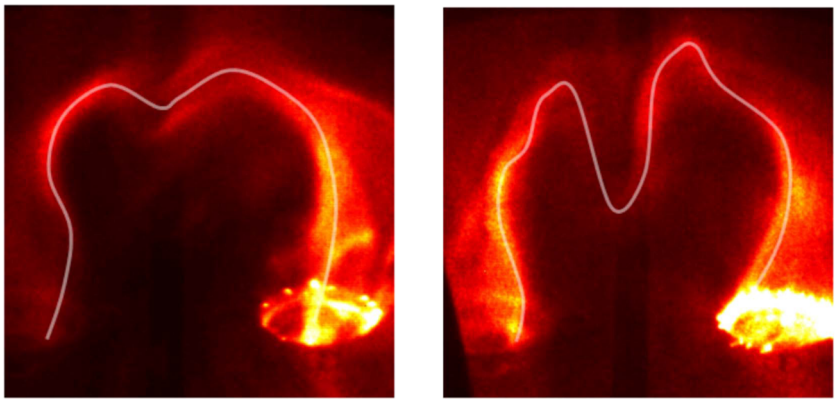

Figure 11. (a) Smooth dip from low injected gas density. (b) Sharp dip from high injected gas density. White lines are hand drawn to indicate axis location (Figure credit: Wongwaitayakornkul et al., 2017).

massive, there is less acceleration resulting in the heavy material lagging, producing a dip. From a mathematical point of view, the solar situation can be considered as characterized by the equation $0 = \mathbf{J} \times \mathbf{B} - \rho \mathbf{g}$, while the lab situation can be considered as characterized by $\rho d\mathbf{U}/dt = \mathbf{J} \times \mathbf{B}$. Thus, if the lab-relevant equation is written as $0 = \mathbf{J} \times \mathbf{B} - \rho d\mathbf{U}/dt$ it is seen that the effective gravity is $d\mathbf{U}/dt$ and that in both the lab and solar situations there will be a dip associated with regions of locally increased ρ.

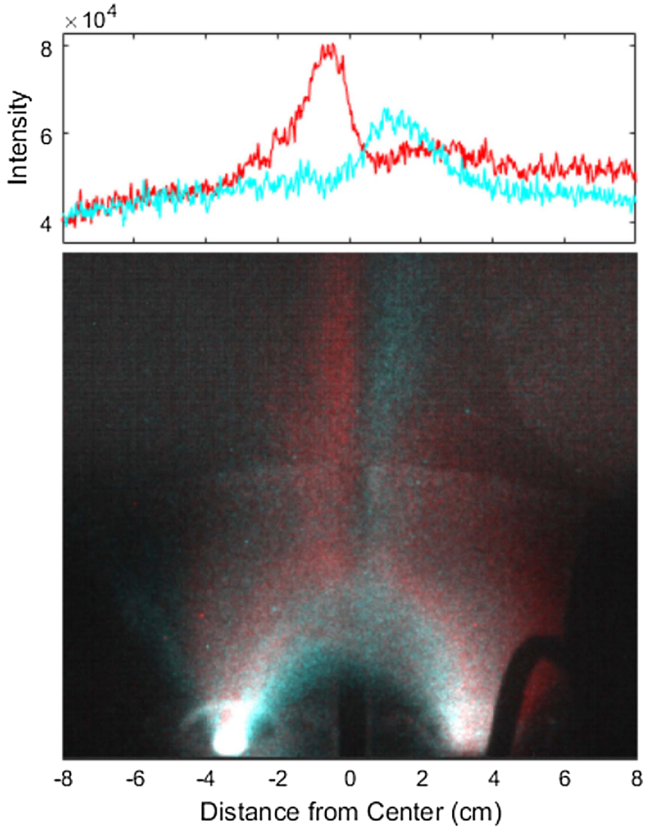

Figure 12. Change in location of dip depending on where density maximum is located. Cyan: higher gas input on right. Red: Higher gas input on left (figure credit: Wongwaitayakornkul et al., 2017).

4.6. Coronal Mass Ejection Cavity

Coronal mass ejections are eruptive solar events having a characteristic three part structure consisting of a bright core surrounded by a dark cavity which in turn is surrounded by a bright leading edge; this structure is indicated in Figure 14a. Haw et al. (2018) studied a solar coronal loop experiment where the vacuum chamber was prefilled with low-density neutral gas of a different species from that used to make the loop. The experimental setup is sketched in Figure 15. Filters placed in front of the camera distinguished the laboratory replica of a coronal loop light from that of the background gas. Because the two gas species were different, the background gas plasma (hydrogen) could be represented as blue and the laboratory replica coronal loop (argon) could be represented as red in the computer-created composite images of the experimental measurements shown in Figure 14b.

The outstanding feature of these measurements is the appearance of a dark gap between the red loop and the adjacent bright blue feature which is parallel to the red loop. The bright blue region was determined to be a reverse current region, that is, a region where the electric current density J_y has the opposite sense of the current density in the laboratory replica coronal loop; the coordinate system in Figure 15 defines the y direction. J_y was determined by combining Ampere's law, the overall structural motion at a vertical velocity v_z and the much stronger dependence of B_x on z than B_z on x to give $\mu_0 J_y = \partial B_x/\partial z - \partial B_z/\partial x \simeq \partial B_x/\partial z \simeq v_z^{-1} \partial B_x/\partial t$.

The reversed current develops because the exterior region plasma (blue) is a magnetic flux conserver, so a reversed current is required to shield the magnetic field produced by the red current. The reversed current is essentially like the eddy current induced on the surface of a copper sheet next to

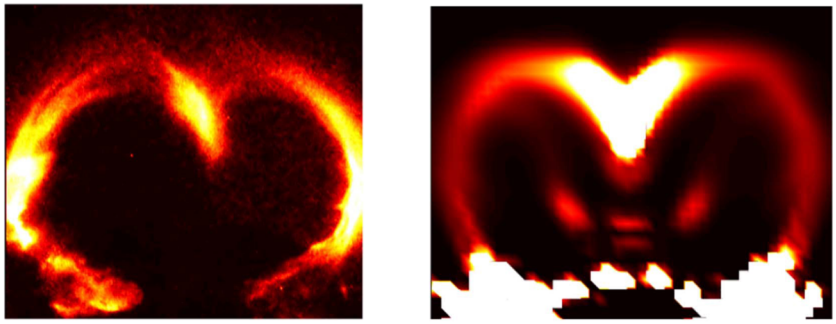

Figure 13. (a) Photograph of experimental loop. (b) Synthetic photograph of numerical simultion of loop from 3-D MHD code (figure credit: Wongwaitayakornkul et al., 2017).

a pulsed wire. The eddy current creates a magnetic field equal and opposite to the field from the wire in order to have no net magnetic field in the copper sheet. Because antiparallel currents mutually repel, the blue current is repelled by the red current leaving a void or cavity in between. Langmuir probe measurements of density show a density depletion in the region between the red and blue currents. A 3-D numerical MHD model produces synthetic images as shown in Figure 14c similar to both those of the experiment and an actual CME. In addition to the experimental and numerical results Haw et al. (2018) also provide an analytic model for this repulsion associated with flux conservation in the external region.

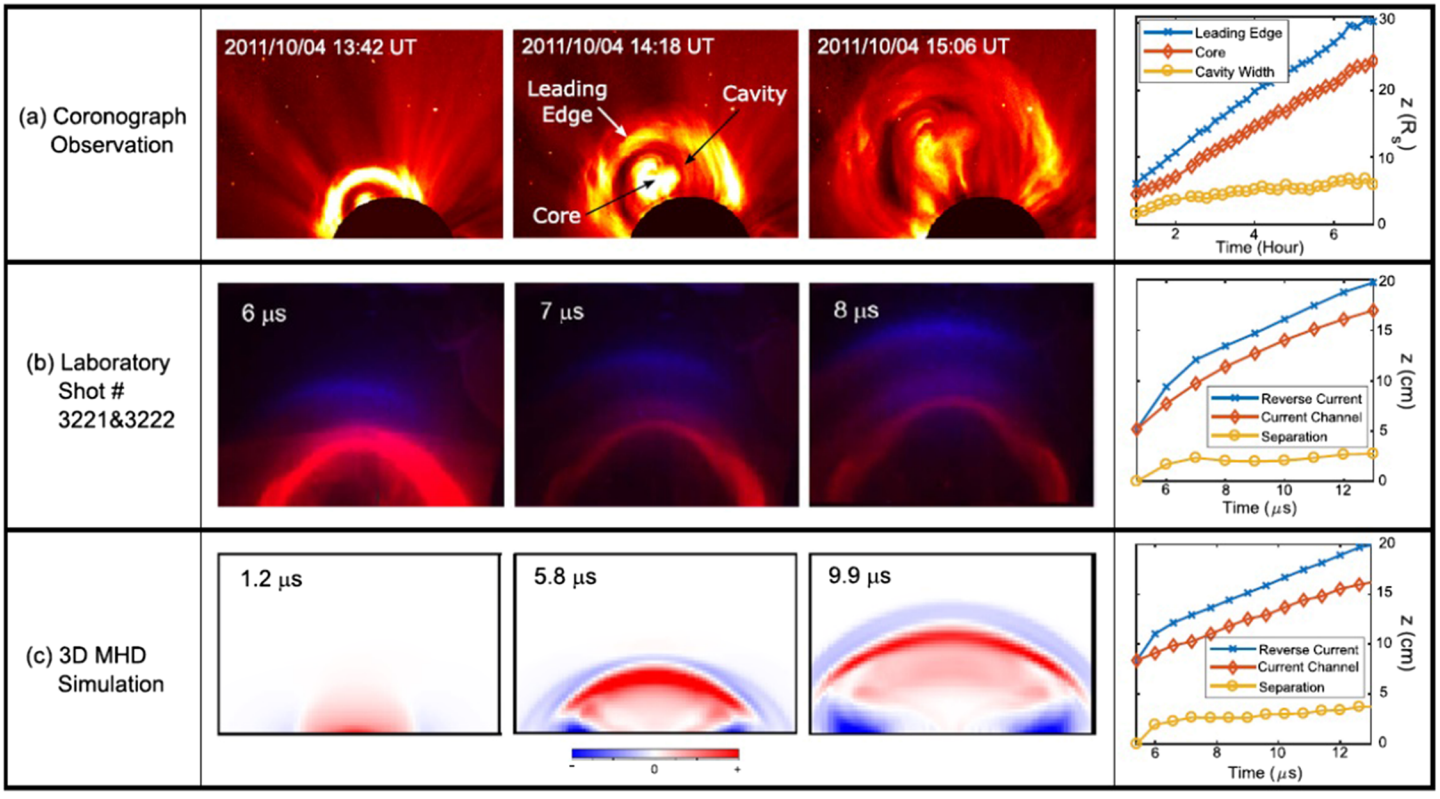

Figure 14. (a) Coronal mass ejection observed on the Sun. (b) Photos of laboratory experiment showing argon loop (red) expanding into hydrogen background plasma (blue). (c) Numerical simulation from 3-D MHD code (figure credit: Haw et al., 2018).

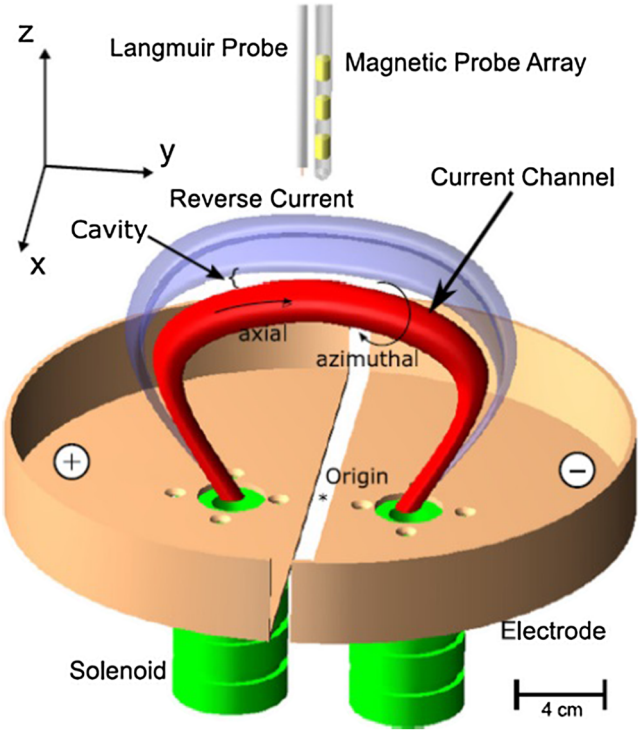

Figure 15. Setup of lab plasma showing loop current (red) and induced reverse current (blue) (figure credit: Haw et al., 2018).

The motion of the blue reversed current into the background plasma corresponds to the blue reversed current acting like a fast-moving piston that compresses the background plasma. Wongwaitayakornkul et al. (2019) have shown that this piston motion can drive a shock wave in the background plasma and have proposed this CME-driven shock as an explanation for the EUV waves (Long et al., 2017) that are often seen in association with CMEs.

4.7. Loss of Confinement of Energetic Particles From Flux Ropes

Tripathi et al. (2007) observed in certain situations that a diffuse plasma jet shot upward from the apex of a laboratory experiment replica of a solar corona loop. This was interpreted by Tripathi et al. (2007) to be a particle orbit phenomenon and so was called a "kinetic jet." The kinetic jet was shown to be closely related to a situation well known in the context of neutral beam injection into a tokamak. In the tokamak context, an injected neutral beam quickly becomes ionized and so turns into an ion beam. The injected neutral beam can be arranged to be either parallel or antiparallel to the tokamak toroidal current (coinjected or counterinjected), and so the resulting ion beam is either parallel or antiparallel to the toroidal electric current. Ion beams produced in a tokamak by counterinjected neutral beams are observed to have much worse confinement than those of coinjected neutral beams; this behavior is supported by numerical particle orbit calculations (e.g., see Mikkelsen et al., 1997).

Although the beam confinement and toroidal current configuration are essentially identical in the laboratory replica of a solar corona loop and a tokamak the means for producing the toroidal current differ. In a tokamak, the toroidal current in the plasma is established when the primary current of a so-called Ohmic heating transformer changes and attempts to change the magnetic flux linked by the toroidal plasma; the plasma toroidal current can be considered to be the one-turn secondary of the Ohmic heating transformer and this plasma current is such that its associated magnetic flux is equal in magnitude and opposite in sign to the flux change introduced by the Ohmic heating transformer. By this means the net flux linked by the tokamak toroidal plasma remains constant corresponding to there being no net toroidal electric field in the plasma. The laboratory experiment replicating a solar loop differs from a tokamak by being a half rather than full torus and instead of having an Ohmic heating transformer drive the toroidal current, the solar loop experiment has electrodes at the foot points drive the toroidal current. In this case the toroidal current is directly imposed by the external power supply (capacitor bank) connected across the electrodes; this power supply is represented by the red cylinder at the bottom in Figures 1b–1d. Although there is an electrostatic potential drop going from one electrode to the other, there is no axial electric field to the extent that ideal MHD is valid because the axial electric field is given by $E_{axial} = -\partial V/\partial s - \partial A_{axial}/\partial t$ which is 0 because $\partial A_{axial}/\partial t = -\partial V/\partial s$ where A_{axial} is proportional to the magnetic flux associated with the axial current. The increase of A_{axial} with time corresponds to the flux tube twisting up as the axial current increases. Thus, while the electrostatic potential drop is real and measurable it does not produce an electric field in the plasma because the electric field contribution produced by the electrostatic potential gradient is exactly canceled by the inductive component of the electric field. From the point of view of the external power supply, it is as if this power supply were switched to be across an inductor so that the power supply voltage would appear across the inductor and this voltage would correspond to $d/dt(LI)$. The wire in the inductor would be perfectly conducting, so there would be no electric field in this wire as the inductive component of the electric field would exactly cancel the electrostatic component. The electric current corresponds to a difference between the electron and ion mean velocities and is independent of the mass-weighted mean of these velocities, that is, independent of the center of mass motion of the plasma.

The kinetic jet shooting up from the apex of the laboratory simulation of a solar loop is explained starting with the concept that upward MHD-driven jets originate from both foot points as sketched in Figure 4 and in Figure 1b; the Doppler blue shifts of these jets are shown in Figure 6. This means that one of the

MHD-driven jets is parallel to the electric current, while the other is antiparallel. The ions in these jets can be considered to be ion beams, and so one ion beam is parallel to the loop axial electric current, while the other is antiparallel. For simplicity, the flux rope will now be assumed to have a straight axis as sketched in Figure 4. Thus, the magnetic field is of the form $\mathbf{B} = B_z\hat{z} + B_\phi\hat{\phi}$. Consider an ion that has an initial infinitesimal radial displacement from the z axis and an initial velocity $\dot{\mathbf{r}} = v_0\hat{z}$ with no initial r or ϕ velocity components. The radial component of the Lorentz equation $m\ddot{\mathbf{r}} = q\dot{\mathbf{r}} \times \mathbf{B}$ can then be written as

$$m(\ddot{r} - r\dot{\phi}^2) = q\left(r\dot{\phi}B_z - v_z B_\phi\right). \tag{11}$$

If both $B_\phi = 0$ and $\ddot{r} = 0$ are assumed, Equation 11 reduces to $\dot{\phi} = -qB_z/m$, that is, to cyclotron motion. Now suppose that $B_\phi \neq 0$ and again assume $\ddot{r} = 0$ in which case Equation 11 can be expressed as

$$\dot{\phi}^2 + \Omega\dot{\phi} - v_z\frac{\Omega B_\phi}{B_z r} = 0 \tag{12}$$

where $\Omega = qB_z/m$. Equation 12 is a quadratic equation in $\dot{\phi}$ with solutions

$$\dot{\phi} = \Omega\frac{-1 \pm \sqrt{1 + 4\dfrac{B_\phi}{B_z}\dfrac{v_z}{\Omega r}}}{2}. \tag{13}$$

If $1 + 4B_\phi v_z/(B_z\Omega r) < 0$ then Equation 13 has no real solution which means it was incorrect to assume $\ddot{r} = 0$. This situation occurs if v_z has the opposite sign of B_ϕ and has magnitude

$$|v_z| > \frac{1}{4}\left|\frac{qB_z^2}{mB_\phi}r\right|. \tag{14}$$

Examination of Equation 11 shows that large positive $-v_z B_\phi$ causes $\ddot{r}$ to become large and positive, so the ion is ejected radially from the flux rope. Numerical calculations of ion trajectories in Tripathi et al. (2007) show indeed that if v_z has the opposite sign of B_ϕ and also has sufficiently large magnitude to satisfy Equation 14, ions are radially ejected from the flux rope. A Hamiltonian analysis involving effective potentials arrives at the same conclusion by showing that an effective potential valley becomes an effective potential hill resulting in loss of radial stability. Having the opposite sign of B_ϕ corresponds to the ion moving counter to the axial current, that is, like a just-ionized counterinjected tokamak neutral beam. The radial ejection can be interpreted equivalently as resulting from the property that opposite currents repel since if v_z has the opposite sign of B_ϕ, the ions with this v_z can be considered as a subcurrent opposite to the main current.

Tripathi et al. (2007) conducted a set of experiments having different gas puff pressures. The different pressures produced correspondingly different jet velocities from the foot points with lower pressures resulting in faster jets since the jet velocity is inversely related to the jet mass for a given force. It was observed that the kinetic jet originating from the apex only occurred when the jet was sufficiently fast. The escape was from the apex because confinement is weakest at the apex. Numerically calculated ion orbits for positive and negative v_z show radial unstable motion for sufficiently large negative v_z. If a uniform current density is assumed then $B_\phi = \mu_0 J_z r/2$, so Equation 14 can be expressed as

$$|v_z| > \frac{1}{2}\left|\frac{qB_z^2}{m\mu_0 J_z}\right|. \tag{15}$$

The ratio of axial current $I = J_z\pi r^2$ to axial flux $\Phi = B_z\pi r^2$ in the flux rope can be expressed using

$$\lambda = \frac{\mu_0 I}{\Phi} = \frac{\mu_0 J_z}{B_z} \tag{16}$$

which is closely related to a force-free equilibrium $\nabla \times \mathbf{B} = \lambda\mathbf{B}$, the difference being that Equation 16 pertains only to the axial components of the magnetic field and current, whereas the force-free equilibrium involves all components. Equation 15 can then be expressed as

$$\left|\frac{\lambda v_z}{\Omega}\right| > \frac{1}{2} \tag{17}$$

which is analogous to a finite Larmor radius condition since v_z/Ω is analogous to a Larmor radius. Since the LHS of this criterion scales as B_z^{-2}, Equation 17 could only be satisfied in solar contexts having very fast ions and extremely weak magnetic fields. This might happen when energetic ions move near a magnetic null.

4.8. Kink Instability Driving Secondary Rayleigh-Taylor Instability

The coaxial jet experiment is similar to the laboratory replica of a solar corona loop but has a coaxial geometry as shown in Figure 3. The jet can be considered a lengthening flux rope with a magnetic field given by $\mathbf{B} = B_z\hat{z} + B_\phi\hat{\phi}$. The jet kinks when it attains a critical length satisfying the Kruskal-Shafranov kink instability criterion (Kruskal & Tuck, 1958; Shafranov, 1970). This criterion is essentially $\mathbf{k}\cdot\mathbf{B} = 0$ where a perturbation $\exp(ik_z z + im\phi)$ is assumed and $k_z\hat{z} + (m/a)\hat{\phi}$ where $k_z = 2\pi/l$, l is the jet length, and a is the jet radius. For B_ϕ/B_z positive it is necessary to have negative m and the Kruskal-Shafranov analysis shows that $m = -1$ is the unstable mode. Thus, the kink instability criterion can be expressed as $q = 2\pi a B_z/(lB_\phi)$ where

$$q = 1 \text{ for instability} \tag{18}$$

$$q > 1 \text{ for stability.} \tag{19}$$

q is known as the "safety factor" in tokamak terminology. The jet has increasing length, so l starts out small in which case q initially exceeds unity and the jet is stable. When the jet attains the critical length at which q drops to unity, the kink instability begins as seen at 10 μs in Figure 3 and as has been verified in detail by Hsu and Bellan (2003). The kink instability grows exponentially and causes the jet to develop an exponentially growing corkscrew shape. An observer attached to the jet plasma would thus be displaced with exponentially increasing distance from the jet axis and so have an exponentially increasing velocity. The observer would therefore be accelerating and since gravity is the same as acceleration, the observer would experience an effective gravity like a passenger in an accelerating automobile.

The effective gravity sets the stage for another type of MHD instability, the magnetic Rayleigh-Taylor instability (RTI) (Chandrasekhar, 1961; Kruskal & Schwarzschild, 1954), which is an extension of the conventional fluid RTI. The RTI takes place at the interface separating a heavy fluid on top of a light fluid. Because of gravity, at the interface ripples develop that cause portions of the heavy and light fluids to interchange and so lower the overall gravitational potential energy. Moser and Bellan (2012) observed that the effective gravity produced by the kink lateral acceleration resulted in a spontaneous development of RTI ripples. They further saw that this caused a change of the jet magnetic field corresponding to phenomena beyond the scope of ideal MHD, namely, a magnetic reconnection as well as an abruptly starting emission of radio waves in the whistler regime. Because whistler waves are at frequencies above the lower hybrid frequency and below the electron cyclotron frequency, whistler waves are in a frequency regime much higher than the MHD frequency regime which consists of frequencies much below the ion cyclotron frequency. Chai and Bellan (2013) observed that there was an enhancement of EUV emission at the location of the RTI, a dimming of visible light emission, and further characterized the emission of whistler radiation. Marshall et al. (2018) observed X-ray bursts coincident with the RTI. Thus, there is a well-defined sequence of jet formation, jet kinking, and then kink-instigated RTI; coincident with the RTI there is enhanced EUV emission, visible light dimming, whistler radiation, and an X-ray burst.

The RTI consists of the small ripples indicated by the white arrows in Figure 16a. A critical feature of the instigation of RTI by kink lateral acceleration is an inherent asymmetry because of the directed nature of the effective gravity. This asymmetry means that ripples develop only on the trailing side of the laterally accelerating jet (bottom side of jet in Figure 16a) with the result that the cross section A of the jet is periodically choked. This periodic choking has the consequence that the axial current density J must increase at the locations of decreased cross section since $J = I/A$ where I is the electric current flowing along the jet. According to ideal MHD, a plasma is a perfect conductor, that is, according to ideal MHD a plasma can

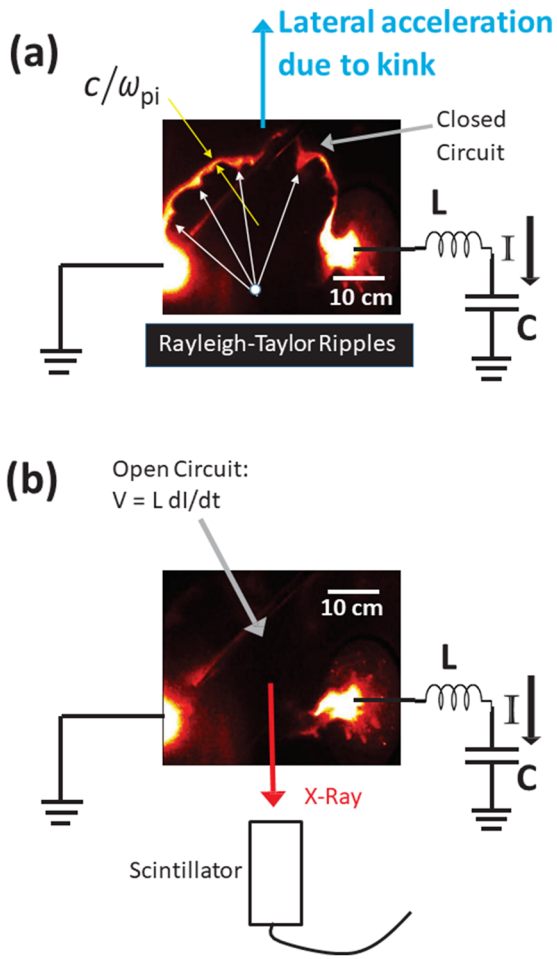

Figure 16. (a) Segment of kinked jet; kink is large arch. Small ripples on inboard side are Rayleigh-Taylor instability. Dimming at Rayleigh Taylor instability is evident. The inductance in the rest of the jet circuit and the capacitor bank are sketched as circuit elements. (b) The Rayleigh-Taylor instability interrupts the current, so there is an inductive voltage drop $V = LdI/dt$ that accelerates a small cohort of electrons to energies where they radiate X-rays which are observed by a plastic scintillator (reproduced from Marshall et al., 2018, with permission from AIP Publishing).

support infinite J. However, just like a real, finite-dimension water pipe cannot carry an infinite number of liters per second, the presumption that a real plasma can carry an infinite J must fail at some physical limit where some physical phenomenon develops and impedes the relative motion between electrons and ions that constitutes the current. This limit is quantified by a ceiling on the electron drift velocity which is the mean electron velocity observed in a frame where the mean ion velocity is 0. If the jet axis defines the z direction, the axial electric current density is $J_z = ne(u_{iz} - u_{ez})$ and so the electron drift velocity is then $v_d = J_z/(ne) = I/(neA)$; the reduction of the current cross section A will thus increase v_d. The theory underlying plasma electrical resistivity is based on the assumption that v_d is small compared to all characteristic plasma velocities, that is, v_d is assumed small compared to the ion acoustic velocity $c_s = \sqrt{\kappa T_e/m_i}$, the electron and ion thermal velocities, $v_{T\sigma} = \sqrt{2\kappa T_\sigma/m_\sigma}$, the phase velocities ω/k_z of any plasma wave, and the speed of light. If v_d approaches any of these characteristic velocities, phenomena occur that cause the plasma to cease acting as a perfect conductor. For example if v_d approaches the ion acoustic velocity, ion acoustic waves become destabilized, whereas if v_d approaches the electron thermal velocity then the electrons run away (Dreicer, 1959). A closely related issue concerns scale lengths. The ideal MHD Ohm's law $\mathbf{E} + \mathbf{U} \times \mathbf{B} = 0$ gives Equation 1a and is based on the assumption that Hall and electron inertia terms can be dropped from the generalized Ohm's law. The argument for dropping these terms is based on the characteristic scale length being larger than the ion skin depth $d_i = c/\omega_{pi}$. The RTI is experimentally observed to squeeze the jet radius to be of the order of d_i which implies that Hall and electron inertia terms will abruptly become important. These terms are associated with fast collisionless reconnection and also with whistler waves (see Chapter 19 in Bellan, 2018c). This squeezing of the flux rope to the d_i scale by the kink-instigated RTI has recently been reproduced numerically by Wongwaitayakornkul et al. (2020) in a 3-D numerical solution of the MHD equations.

The experimental observations indicate that waves are destabilized when the RTI ripples choke the current channel cross section. Preliminary measurements indicate that the waves are in the whistler regime. The jet behaves as if a large resistor were spliced into the axial current circuit at the location of the RTI ripples and this causes several associated phenomena. First, there is a pronounced dimming of visible light emission at the ripple location as seen in Figure 16a. At the same time and location there is an increase in EUV radiation as reported in Chai and Bellan (2013). The visible light dimming indicates that density is depleted at the RTI location and the enhanced EUV emission indicates simultaneous electron acceleration to high energy followed by collisions with ions to produce ions in highly excited states, the decay of which radiates the EUV emission. These two effects suggest that at the RTI location a large inductive voltage drop LdI/dt is established in a direction such as to sustain the current flow. This LdI/dt voltage drop is indicated in Figure 16b. Since the jet originates from a negative electrode, conventional current flows toward the electrode, and so in accordance with Lenz's law the electric field providing the LdI/dt voltage drop points toward the electrode to oppose the change in current. Thus, in Figure 16 the jet flows to the left and the inductive electric field points to the right. However, ions and electrons constituting the jet both flow to the left, away from the electrode; this is consistent with a rightward electric current direction by having the leftward electron flow velocity exceed the ion leftward flow velocity. The rightward direction of the inductive field will accelerate ions to the right and electrons to the left. Thus, the inductive electric field reduces the ion leftward flow velocity leading to density depletion at the RTI location and increases the electron leftward flow velocity leading to

generation of energetic electrons that can produce EUV emission in the region of density depletion. It should be noted that the electron motion is not governed by a complete equation of motion, that is, by a description of how forces change the electron momentum. Instead, the electron mass is assumed to be infinitesimal and consistent with the characterization of the plasma by the MHD equations, the electron velocity adjusts in such a way as to produce the electric current required by the combination of boundary conditions (axial current) and Maxwell's equations (azimuthal current). This setting to 0 of the electron inertia is consistent with treatments of ideal perfect conductors and fails to take into account physics taking place on the length scale of the electron skin depth $d_e = c/\omega_{pe}$ and on the timescale of the electron plasma and cyclotron frequencies ω_{pe}, ω_{ce}.

This model of a large inductive voltage drop leading to oppositely directed ion and electron accelerations is closely related to the double layer concept proposed by Alfvén (1986) to describe the explosive inductive mechanism described by Alfvén and Carlqvist (1967) and by Jacobsen and Carlqvist (1964). The mechanism is explosive because all inductive energy of an initially zero resistance system is dissipated at the localized small segment of an inductive circuit where the electrical resistance becomes finite for some reason. This is seen from the circuit equation $IR + LdI/dt = 0$ where R is the resistance of the localized region; multiplying by I and integrating gives $\int I^2 R dt = -LI^2/2$.

Using a plastic scintillator, Marshall et al. (2018) observed a ~1 μs burst of ~6 keV X-rays coincident with the RTI. This short X-ray burst is interpreted as resulting from a small cohort of electrons being collisionlessly accelerated to the full LdI/dt voltage drop (Marshall & Bellan, 2019). Although the mean free path of the thermal electrons is only a few microns for the 2 eV temperature and high density of the jet which has a length of tens of cm, statistical analysis shows that a small cohort of electrons can nevertheless be collisionlessly accelerated to high energy. The statistical argument is based on the fact that when an electron travels a collision mean free path, it has a $1 - e^{-1} = 0.63$ probability of being scattered and so lose its directed momentum. However, this means that the electron has an $e^{-1} = 0.37$ chance of not being scattered. If one considers the 0.37 fraction of the electrons that are not scattered, because these electrons are accelerated by the electric field after one mean free path their kinetic energy will have increased. Since mean free path is quadratically proportional to electron kinetic energy, the mean free path for these unscattered electrons becomes larger. When this group of electrons travel the next, longer mean free path, again a 0.37 fraction will not scatter and these will develop an even longer mean free path. This process repeats, so that ultimately a fraction e^{-N} of the electrons will have collisionlessly traveled N successive increasingly long mean free paths. Eventually these electrons will undergo a large angle collision and because of the rapid deceleration will emit X-rays. Thus, there will be a brief transient burst of X-rays as observed.

4.9. Whistler Wave Emission Associated With Kink-Driven RTI

The choking of the current channel to the ion skin depth by the kink-driven RTI resulted in phenomena beyond the scope of ideal MHD, namely, a burst of X-rays, evidence of waves in the whistler regime, and a change in the magnetic topology indicating magnetic reconnection. The generalized Ohm's law,

$$\mathbf{E} + \mathbf{U}\times\mathbf{B} - \underbrace{\frac{\mathbf{J}}{ne}\times\mathbf{B}}_{\text{Hall}} + \underbrace{\frac{1}{ne}\nabla P_e}_{\text{electron pressure}} + \underbrace{\frac{m_e}{e}\frac{d\mathbf{u}_e}{dt}}_{\text{electron inertia}} = \underbrace{\eta\mathbf{J}}_{\text{resistive}} \tag{20}$$

is essentially a rearrangement of the two-fluid electron equation of motion and contains the electric field $\mathbf{E}$ as one of its terms. Here $\mathbf{U}$ is the center of mass velocity of the plasma, $\mathbf{u}_e = \mathbf{U} - \mathbf{J}/ne$ is the mean velocity of the electrons, and all quantities are measured in the lab frame. On taking the curl of the generalized Ohm's law and invoking Faraday's law $\nabla\times\mathbf{E} = -\partial\mathbf{B}/\partial t$ a generalized form of the induction equation results (see Sec.19.2 of Bellan (2018c) for a more detailed discussion). As discussed in section 2 a reference Alfvén velocity $v_{A0} = B_0\sqrt{\mu_0\rho_0}$ can be defined on choosing a reference magnetic field strength B_0 and a reference mass density ρ_0. Then, also as discussed in section 2, by additionally choosing a reference scale length l_0, a reference time $\tau_{A0} = l_0/v_{A0}$ is established. On defining normalized quantities $\overline{\mathbf{B}} = B/B_0$, $\bar{t} = t/\tau_{A0}$, $\overline{\mathbf{U}} = \mathbf{U}/v_{A0}$, and $\bar{\rho} = \rho/\rho_0$ the normalized induction equation becomes (Bellan, 2018c)

$$\frac{\partial \overline{\mathbf{B}}}{\partial \bar{t}} = \overline{\nabla} \times \left(\overline{\mathbf{U}} \times \overline{\mathbf{B}}\right) + \underbrace{\frac{1}{S}\overline{\nabla}^2\overline{\mathbf{B}}}_{\text{resistive}} - \underbrace{\frac{d_i}{l_0}\overline{\nabla} \times \left[\left(\overline{\nabla} \times \overline{\mathbf{B}}\right) \times \overline{\mathbf{B}}\right]}_{\text{Hall}} + \underbrace{\frac{d_i}{l_0}\overline{\nabla} \times \left(\frac{1}{\overline{\rho}}\overline{\nabla}\beta_e\right)}_{\text{electron pressure}} - \underbrace{\frac{d_e^2}{l_0^2}\overline{\nabla} \times \frac{\partial\left(\overline{\nabla} \times \overline{\mathbf{B}}\right)}{\partial \bar{t}}}_{\text{electron inertia}} \tag{21}$$

where

$$d_i = \frac{c}{\omega_{pi}}, \quad d_e = \frac{c}{\omega_{pe}} \tag{22}$$

are the ion and electron collisionless skin depths and

$$S = \frac{l_0 \mu_0 v_A}{\eta} \tag{23}$$

is the Lundquist number. Collisionless skin depths and Lundquist numbers for the Caltech experiment, the solar corona, and the solar chromosphere are listed in Table 2; these are calculated from the respective parameters listed in Table 1. The ideal MHD Ohm's law, Equation 1b, results when the terms labeled resistive, Hall, electron pressure, and electron inertia are all dropped. Resistive MHD results when the term involving S is retained, while the Hall, electron pressure, and electron inertia are dropped. The finite value of S in resistive MHD enables magnetic reconnection (change of magnetic topology) to occur but the timescales predicted by resistive MHD are generally much slower than what is observed (Bhattacharjee et al., 2001). As can be seen from the form of the resistive term in Equation 21, the resistive term (term involving S) is diffusive in nature. When the scale length l_0 shrinks to be of the order of the ion skin depth d_i, so d_i/l_0 becomes of order unity, the Hall term becomes important and changes the structure of the equation in a very significant manner as it introduces a cross-coupling between different components of the magnetic field; this cross-coupling does not exist in ideal or resistive MHD. Unlike the resistive term (term involving S), the Hall term is not diffusive but instead is the fundamental term enabling whistler waves; these waves result from the cross-coupling between different components of the magnetic field mentioned above. In fact, the basic dispersion relation for whistler waves can be derived by retaining only the LHS of Equation 21 and the Hall term and then linearizing these equations about a uniform background magnetic field. In the reconnection situation, the background magnetic field is very nonuniform and represents a current sheet or in three dimensions a flux rope, so the situation is more complicated than that of whistler waves. The current sheet model is 2.5D as it involves vectors that have components in three dimensions but two dimensions of the equilibrium are ignorable (e.g., y and z directions) and all vector components of perturbations depend on only two components; for example, all components of all perturbation vectors might depend on x and on y but not on z. Analysis of Equation 21 in the limit where the Hall term dominates the RHS shows there is a fast nondiffusive reconnection which takes place on the whistler timescale and where there is some generation of whistler waves (Yoon & Bellan, 2017, 2019a) as whistler waves are the uniform magnetic field normal mode. A peculiar and identifying feature of whistler waves is that as a consequence of the cross-coupling of magnetic field components whistler waves involve a circularly polarized magnetic field perturbation. Furthermore, and somewhat surprisingly this circular polarization holds even if the wave is propagating obliquely relative to the background magnetic field (Bellan, 2013; Verkhoglyadova et al., 2010). This latter fact indicates that whistler waves should be identifiable even in situations where the direction of the background magnetic field is not known and/or changing over space and time.

The earlier observation of oscillations in the whistler frequency regime (i.e., $\omega_{ci} \ll \omega \ll \omega_{ce}$), the multitude of new transient phenomena that appear when the scale length decreases to be of the order of d_i, and the circular polarization of whistler waves even when oblique suggested that the characteristic circular polarization of whistler waves should be observable when the d_i scale is attained no matter what the direction of the instantaneous average magnetic field might be. Haw et al. (2019) designed, constructed, and used a special radio frequency (rf) magnetic probe that consisted of four separate three-coil clusters arranged to

Table 2
Parameters That Characterize Properties Beyond Ideal MHD

Parameter	Symbol (units)	Caltech Lab	Corona	Chromosphere
Ion skin depth	d_i (m)	8×10^{-3}	2	0.2
Electron skin depth	d_e (m)	3×10^{-5}	5×10^{-2}	5×10^{-3}
Resistivity	η (Ohm-m)	1.7×10^{-4}	2×10^{-6}	3.6×10^{-4}
Lundquist number	$S=l_0\mu_0 v_A/\eta$	43	8×10^{12}	2×10^{8}
Ion-ion collision time	τ_{ii} (s)	10^{-9}	0.03	2×10^{-6}
Electron collision time	τ_e (s)	5×10^{-12}	10^{-3}	5×10^{-8}
e-i energy equipartition time	$\tau_{E,ei}$ (s)	3×10^{-7}	2	10^{-4}
Viscosity (Braginskii)	η_0 (kg m^{-1} s^{-1})	10^{-5}	10^{-2}	10^{-6}
Ion magnetization	$\omega_{ci}\tau_{ii}$	2×10^{-3}	10^{4}	1
Reynolds number	$l_0 v_A\rho_0/\eta_0$	10^{6}	5×10^{4}	2×10^{8}

Note. These are all calculated from the reference parameters given in Table 1.

measure the local vector magnetic field. The four clusters were arranged in a tetrahedron formation so as to provide enough information to calculate the curl of the wave magnetic field $\tilde{\mathbf{B}}$ and hence provide a measurement of the wave current $\tilde{\mathbf{J}}$. The wave vector $\mathbf{k}$ was then determined by inverting Ampere's law $i\mathbf{k}\times\tilde{\mathbf{B}}=\mu_0\tilde{\mathbf{J}}$ using a method described in Bellan (2016b). This was done for each frequency ω in a Fourier transform of the signal, and so $\mathbf{k}(\omega)$ was measured experimentally. Haw et al. (2019) showed that the experimentally measured dispersion relation was in agreement with the theoretical whistler dispersion relation. Haw et al. (2019) also measured the wave $\tilde{\mathbf{B}}(t)$ as a function of time and showed that $\tilde{\mathbf{B}}(t)$ was circularly polarized. Figure 17 shows the physical location of the probe (called quad-probe in the figure), Figure 18 (middle) shows the observed circular polarization of the rf magnetic field, and Figure 19 shows that the measured dispersion relation is in good agreement with the theoretical whistler dispersion (purple shaded region).

4.10. Observation of the Dependence of the RTI Wavelength on Magnetic Field Strength

The RTI results when there is an effective gravity g at the interface between a dense gas and a diffuse gas. In the presence of a uniform magnetic field $\mathbf{B}$ tangential to this interface, the Rayleigh-Taylor growth rate is given by (Goedbloed et al., 2019; Kruskal & Schwarzschild, 1954)

$$\gamma^2 = kg - 2\frac{(\mathbf{k}\cdot\mathbf{B})^2}{\mu_0\rho} \tag{24}$$

where ρ is the density of the dense gas and the density of the diffuse gas is assumed to be negligible. If the wavevector $\mathbf{k}$ is nearly coaligned with $\mathbf{B}$ this becomes

$$\gamma^2 = kg - 2\frac{k^2B^2}{\mu_0\rho} \tag{25}$$

which gives maximum γ^2 when $g=4kB^2/\mu_0\rho$. This relation implies that if $\mathbf{k}$ and $\mathbf{B}$ are along the flux rope axis, the instability wavelength for maximum growth is related to the magnetic field strength by

$$\lambda\rho g = 8\pi B^2/\mu_0 \tag{26}$$

where $\lambda=2\pi/k$. Equation 26 shows that when the axial magnetic field is so strong that λ exceeds the length of the flux rope, it is not possible to fit an entire instability wavelength into the flux rope, and so the flux rope will not have a RTI. However, if the magnetic field is weak, then λ will be short compared to the flux rope length, and so the instability can take place. By operating the bipolar experiment with a relatively small bias magnetic field (axial magnetic field), Zhang et al. (2020) observed RTIs associated with the acceleration provided by the hoop force caused by the current flowing along the arched flux rope. A series of plasma shots was made with different values of bias magnetic field and it was observed that the wavelength λ of the Rayleigh-Taylor ripples increased with the bias magnetic field strength in a manner consistent with Equation 26. Figure 20a shows Rayleigh-Taylor ripples for weak (upper row) and strong

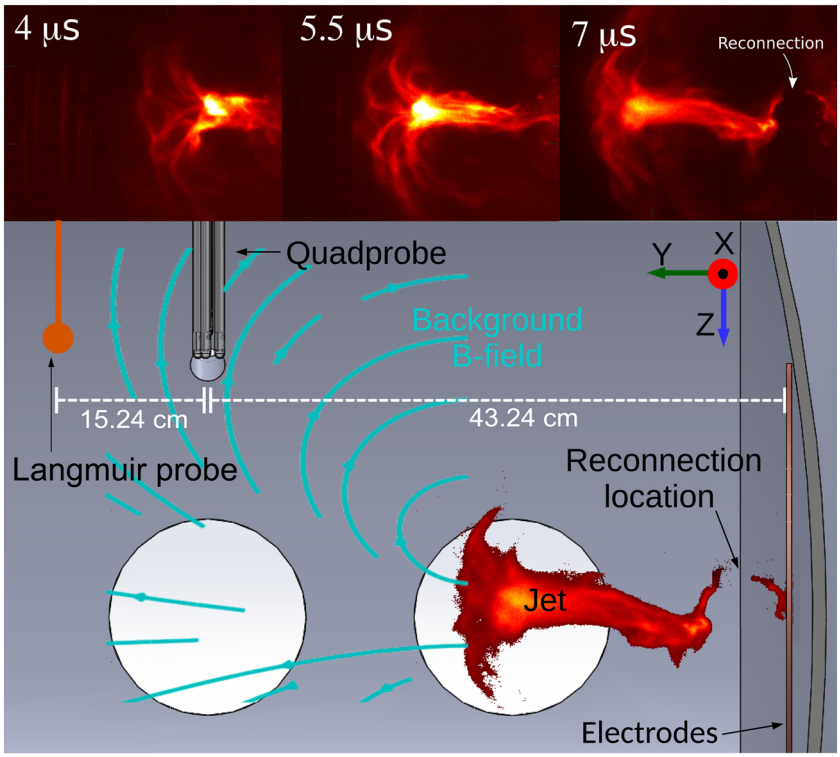

Figure 17. (top) Time sequence of reconnection. (bottom) Location of quadprobe (four-station rf magnetic probe) relative to reconnection region (reprinted figure with permission from Haw et al., 2019; Copyright 2019 by John Wiley and Sons).

(lower row) bias magnetic field strengths; it is seen that the wavelength is longer for the strong bias magnetic field. Figure 20b shows the scaling of λ with the voltage on the capacitor used to drive the bias magnetic field and Figure 20c shows a plot of $s = \lambda\rho g$ versus a parameter proportional to the square of the bias magnetic field (this parameter was mislabeled as y in the figure).

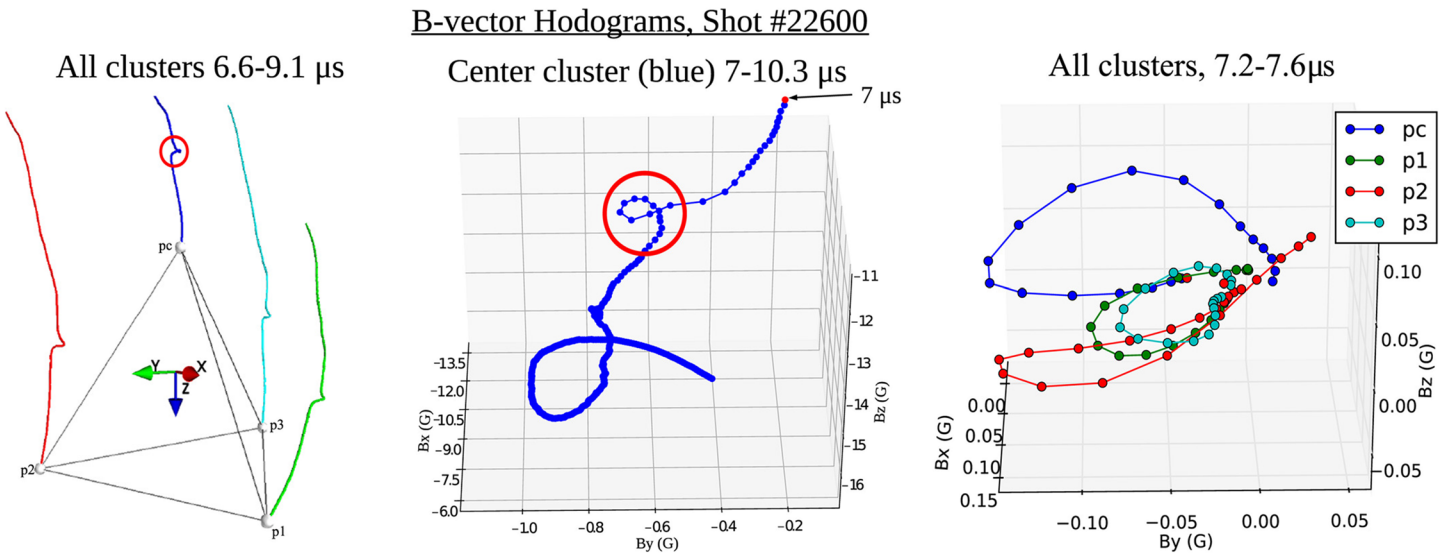

Figure 18. (left) Signals measured by each of four clusters on quadprobe. (middle) Circular polarization of rf magnetic field as observed by middle cluster. (right) Hodographs of all four clusters (reprinted figure with permission from Haw et al., 2019; Copyright 2019 by John Wiley and Sons).

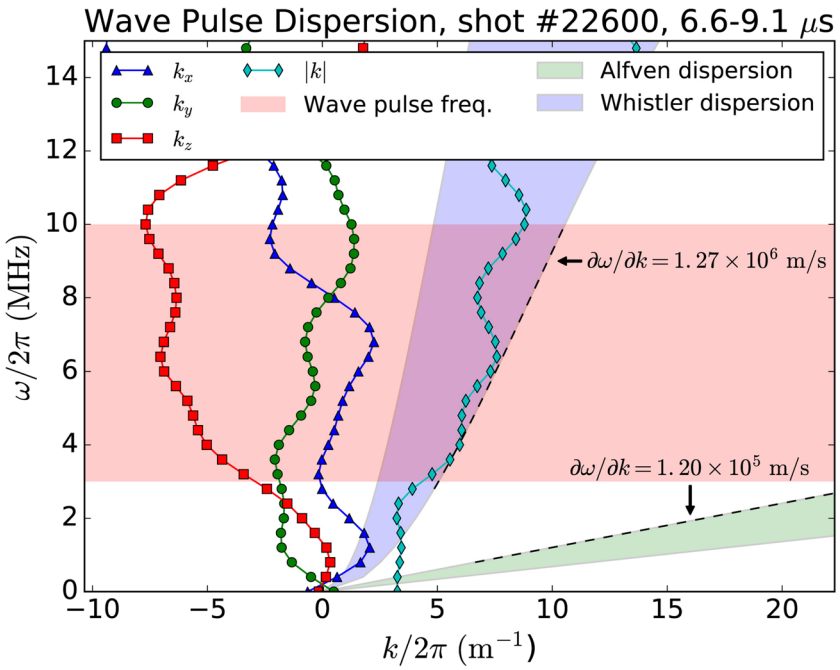

Figure 19. Measured dispersion relation is in agreement with whistler wave (purple shaded region) and much faster than Alfvén wave (green shaded region). (Reprinted figure with permission from Haw et al., 2019; Copyright 2019 by John Wiley and Sons).

4.11. Direct Access to the Ion Skin Depth Scale by the Kink Instability

Section 4.8 described a sequence where lateral acceleration of a flux rope by a kink instability produced a large effective gravity that created the environment of heavy fluid on top of light fluid wherein a Rayleigh Taylor instability developed. The Rayleigh Taylor ripples choked the jet cross section down to the ion skin depth $d_i = c/\omega_{pi}$ which corresponded to the electron drift velocity becoming so large that the assumptions of ideal MHD no longer hold. In particular, the plasma no longer behaved as a perfect conductor and instead behaved as if it had a large resistance. This interrupted the current flowing along the flux rope axis resulting in a large inductive voltage drop, generation of an X-ray burst, and emission of a burst of whistler waves.

By operating the experiment in a somewhat different regime, choking of the flux rope cross section down to d_i was observed by Seo et al. (2020) without the intermediate process of the kink driving a RTI. Here instead, the kink instability directly caused the flux rope cross section to be reduced to be of the order of d_i. The kink instability is an ideal MHD instability which means that the kink cross section is presumed to be larger than d_i since, as comparison between Equations 1b and 21 shows, ideal MHD is based on the assumption that Hall terms can be dropped from the generalized Ohm's law and the condition for dropping these terms is that the scale length l_0 exceeds d_i. However, one of the important properties of the kink instability is that it is an incompressible instability (Newcomb, 1960). The kink process involves the initially straight axis of the flux rope becoming an exponentially growing helix. This process means that the flux rope axis length will increase. However, because kink incompressibility means that the flux rope volume remains constant during the instability, increase of the length of the flux rope axis means that the flux rope cross section must decrease to maintain constant volume. This decrease of flux rope cross section means that the scale length of the cross section can decrease to be less than d_i at which point the Hall term becomes important and ideal MHD no longer holds. Seo et al. (2020) observed this process in the coaxial configuration and saw that the aspect ratio (i.e., length/radius) of a flux rope increased as the flux rope underwent kink instability and that when the radius decreased to be of the order d_i, an X-ray burst, a whistler wave burst, and a change of magnetic topology (magnetic reconnection) occurred simultaneously. The X-ray burst is indicative of the sudden development of a large inductive electric field and is consistent with localized interruption of current because of localized increase in resistivity. The whistler wave burst is indicative that Hall terms are

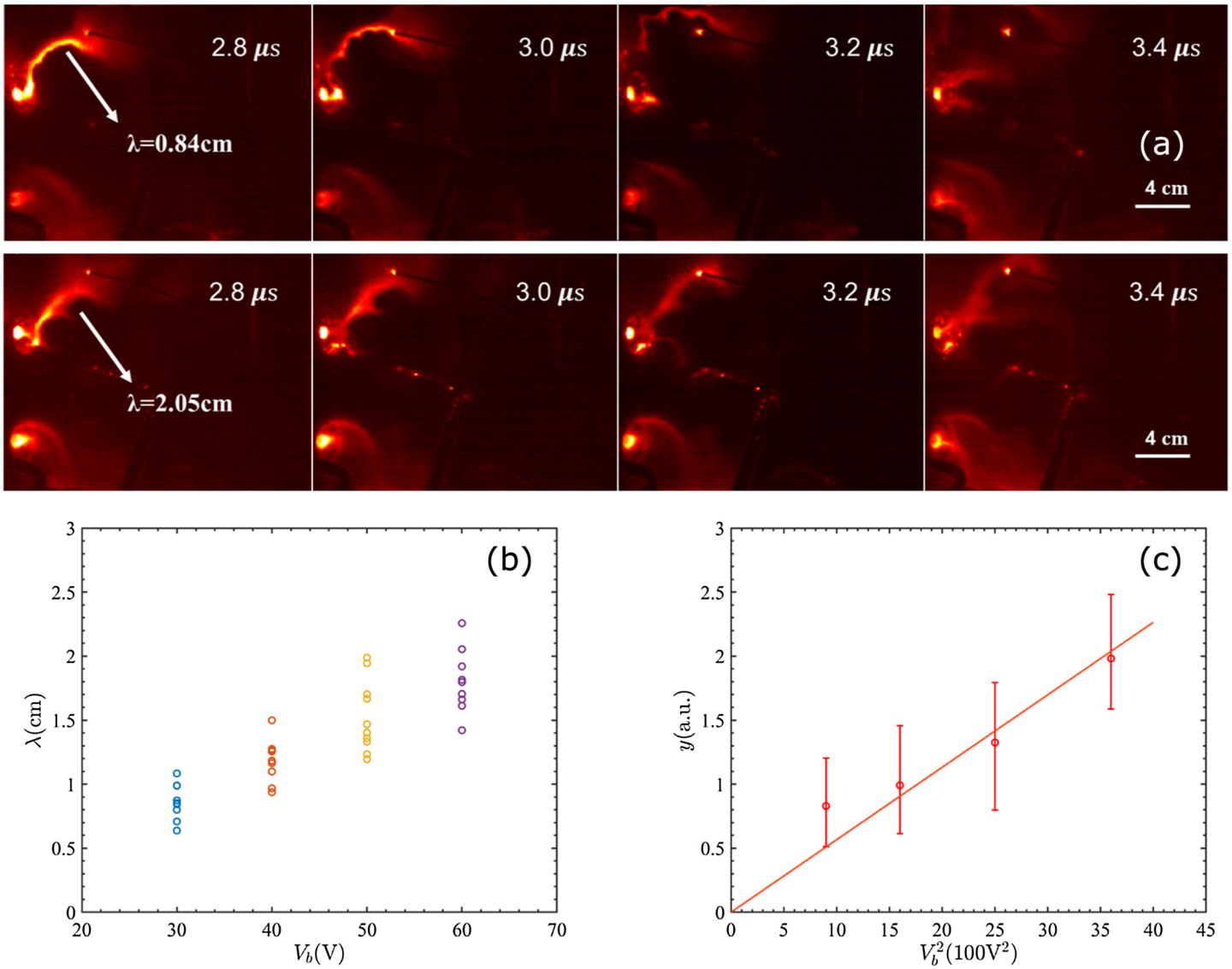

Figure 20. (a) Upper row of photos shows Rayleigh-Taylor evolution when bias field is small; lower row shows evolution when bias field is 2 times larger. Note much longer Rayleigh-Taylor wavelength at 3.0 μs in lower row compared to upper row at the same time. (b) Scaling of Rayleigh-Taylor wavelength with charge voltage on bias field capacitor (bias field is proportional to this voltage). (c) plot of $y = \lambda\rho g$ versus square of bias field voltage; compare with Equation 26 (figure credit: Zhang et al., 2020).

suddenly important as whistler waves are the characteristic mode associated with Hall term dynamics. The sudden change in magnetic topology is indicative of fast magnetic reconnection resulting from Hall and electron inertia terms that are neglected in ideal MHD.

4.12. Transport Considerations

While the experiments have been largely directed toward investigation of ideal MHD physics, many phenomena beyond ideal MHD have been addressed to various extents such as accessing the Hall regime, excitation of whistlers, and X-ray production that have already been discussed. In addition, several issues relating to transport have been considered. While transport is often considered as an afterthought, it ultimately constrains important plasma parameters such as temperature and lifetime. Transport issues can be subtle since collisions between like-sign particles have drastically different consequences from collisions between opposite-sign particles (see section 5.6 in Chen, 1984, and section 2 in O'Neil, 1995). Specifically, ion-ion collisions provide viscosity but have no effect on electrical resistivity and hence no effect on the extent to which magnetic flux is frozen into the plasma. Similarly, ion-ion collisions have no effect on

confinement of the bulk ions in a magnetic field. In particular, the ion-ion collision frequency can greatly exceed the ion cyclotron frequency so that even though no single ion ever completes an ion cyclotron orbit, magnetic flux remains frozen in to the collection of ions and the ions remain confined. Diffusion of the plasma center of mass (which is essentially the ion center of mass because $m_i/m_e \gg 1$) results only from electron-ion collisions in the context of resistive MHD (see section 5.5 of Chen, 1984).

Hydrodynamic concepts such as turbulence associated with a large Reynolds number are not applicable to a low β plasma such as the lab and solar plasmas discussed here. This is because consideration of Reynolds number relates to the competition between the nondiagonal components of the pressure tensor (these components scale as viscosity times velocity shear) and the convective component $\rho\mathbf{U}\cdot\nabla\mathbf{U}$ of the fluid acceleration in the Navier-Stokes equation. However, in MHD the Navier-Stokes equation is replaced by Equation 1a and in low β plasmas such as being considered here the magnetic force term greatly exceeds the divergence of the pressure tensor. The off-diagonal components of the pressure tensor are consequently second-order small since they are small compared to the gradient of the isotropic pressure which itself is small compared to the magnetic force. Since viscosity is essentially a description of how velocity shears create the off-diagonal components of the pressure tensor, viscous forces are relatively unimportant compared to other forces. Thus, while a Reynolds number (comparison of viscous term to convective term) can be calculated, it does not denote any specific regime such as turbulent or nonturbulent in a low β MHD plasma. Essentially, the plasma is well frozen to the magnetic field, and so if the plasma attempted to develop a hydrodynamic-type turbulence it would have to distort the magnetic field which would require more energy than is available in the pressure gradient-driven turbulence. Instead, the plasma stability is characterized by MHD instabilities such as the kink and RTIs which feed off the magnetic energy.

However, it is conceivable that while viscosity is small, it might contribute to heating the plasma by converting velocity shear into heat. The standard plasma transport equations are given by Braginskii (1965). The basic viscosity is $\eta_0 = 0.96 n\kappa T_i \tau_{ii}$ (the use of eta to define viscosity leads to a possible confusion with resistivity which is also defined by eta in standard notation, but rather than change to a different symbol here for either viscosity or resistivity, the use of a subscript will mean viscosity and if there is no subscript then the meaning will be resistivity). Braginskii shows that when $\omega_{ci}\tau_{ii} \gg 1$, the viscosity depends on η_0, η_1, η_2, η_3, and η_4 where η_1, $\eta_2 \sim \eta_0/(\omega_{ci}\tau_{ii})^2$ and η_3, $\eta_4 \sim \eta_0/(\omega_{ci}\tau_{ii})$. The Caltech lab experiment with parameters given in Table 1 has $\omega_{ci}\tau_{ii} \ll 1$ so that in this experiment the viscosity only involves η_0 which is listed in Table 2. Using Equations 2.3i, 2.20, and 2.22 in Braginskii (1965), it is seen that the rate of ion temperature increase as a result of viscous heating is given by

$$\frac{3}{2} n \frac{d}{dt}(\kappa T_i) = \pi_{i\alpha\beta} \frac{\partial u_{i\alpha}}{\partial x_\beta} \tag{27}$$

where if $\omega_{ci}\tau_{ii} \ll 1$

$$\pi_{i\alpha\beta} = -\eta_0 W_{\alpha\beta}. \tag{28}$$

If $\omega_{ci}\tau_{ii} \gg 1$ then $\boldsymbol{\pi}_{i\alpha\beta}$ is given in Braginskii (1965) by a complicated expression involving η_0, η_1, η_2, η_3, and η_4, so since η_0 is larger by at least a factor of $\omega_{ci}\tau_{ii}$ relative to the other components, Equation 28 can be considered an upper bound on the stress tensor. The quantity $W_{\alpha\beta}$ in Equation 28 is a linear function of $\partial u_{i\alpha}/\partial x_\beta$, and so for purposes of estimation we may assume that $W_{\alpha\beta} \approx \partial u_{i\alpha}/\partial x_\beta$. Equation 27 can then be expressed in the form of a bound on the viscous heating as

$$n\left(\frac{d}{dt}(\kappa T_i)\right)_{viscous} < \eta_0 \max\left|\frac{\partial u_{i\alpha}}{\partial x_\beta}\right|^2 \tag{29}$$

or using $\eta_0 \approx n\kappa T_i \tau_{ii}$

$$\frac{1}{T_i}\left(\frac{dT_i}{dt}\right)_{viscous} < \tau_{ii} \max\left|\frac{\partial u_{i\alpha}}{\partial x_\beta}\right|^2. \tag{30}$$

The maximum velocity shear in the experiment is given by the Alfvén velocity divided by the radius of the current channel, so using a current channel radius of $0.01 l_0$ and the ion-ion collision time $\tau_{ii} \simeq 10^{-9}$ s

given in Table 2, Equation 30 gives $\left[\frac{1}{T_i}\left(\frac{dT_i}{dt}\right)_{viscous}\right]^{-1} > 25\,\mu s$ which is longer than the experimental timescale. This analysis thus shows that ion viscous heating will not be important. Furthermore, the assumed $0.01l_0$ radius implies a 3 mm current channel radius for the lab experiment which is an overly conservative assumption as this radius is less than the ion skin depth; at this scale ideal MHD is no longer valid and the whistler-related phenomena discussed in section 4.9 would take place. However, this $0.01l_0$ is being assumed here for consistency with comparison with the solar plasmas where a 100:1 aspect ratio is realistic and also to provide an easily calculable bound for viscous heating. In contrast to the viscous heating time, the electron-ion energy equipartition time for the lab experiment is 0.25 μs which is much shorter than the experimental time. Thus, the electrons heat up from resistive dissipation and then quickly share their thermal energy with ions via electron-ion collisions. Measurements by Perkins (2011) indicated that the Ohmic heating of the electrons (shared via collisions with the ions) in the Caltech lab experiment is balanced by EUV radiation to clamp the temperature to about 2 eV. The measurements by Perkins (2011) also show that the Ohmic heating power is only about 10% of the total input power with the remainder of the input power going into the translational kinetic energy of the expanding loop as well as the increase of magnetic energy in the loop as a consequence of its volume expanding while its internal magnetic field remains approximately constant.

Calculation of ion viscous heating for a solar corona loop having current channel radius of $0.01l_0$ shows that the ion viscous heating time is 1 s which is approximately the same as the electron-ion energy equipartition time; however, the estimate for the RHS of Equation 29 is probably excessive since actual velocities will generally be less than v_A, the more complicated expressions involving η_1–η_4 should be used, and η_1–$\eta_4 \ll \eta_0$. The possibility that ion viscous heating can in certain circumstances play a role comparable to resistive heating in coronal loop plasmas has been shown by Ofman et al. (1994) and by Erdelyi and Goossens (1995).

Calculation for the solar chromosphere assuming again a current channel radius of $0.01l_0$ shows that the ion viscous heating time is of the order of 700 s which greatly exceeds the electron-ion equipartition time of 10^{-4} s. Thus, just as in the lab experiment, ion viscous heating is likely to be dominated by ion heating via electron-ion energy equipartition in both solar corona loops and in the chromosphere.

The Reynolds numbers for the lab experiment, solar corona loop, and chromosphere are listed in Table 2, but as mentioned earlier these have no real meaning in the context of low β MHD because low β means that MHD forces generally dominate pressure gradient terms including the off-diagonal terms associated with viscosity.

4.13. Experimental Results Motivating New Theoretical Models

The experimental results discussed here revealed new behaviors that had not been predicted in any theoretical model, and so in order to explain the observations, new models were developed. In addition, simply working in the general topical area often motivated development of new models even without a specific experimental result. These models are not only relevant to solar physics, but also to magnetospheric physics and to astrophysics which can have similar physics but at very different scales from the lab or the Sun. Examples of such theoretical models are the following:

1. A model showing why flux ropes tend to be collimated (Bellan, 2003)
2. A model for how accretion disks and astrophysical jets form a complete electric circuit that transfers angular momentum in a conservative way much like a generator transfers angular momentum via wires to a distant motor (Bellan, 2016a, 2018d)
3. A model providing a time-dependent analytic solution for an astrophysical jet (Bellan, 2020)
4. A model for how energetic particles are created in the presence of sub-Dreicer electric fields (Marshall & Bellan, 2019)
5. A model providing an intuitive explanation for fast collisionless magnetic reconnection (Yoon & Bellan, 2017, 2019a) in the electron MHD context, that is, the context where the timescale is so fast that ions can be considered stationary, and the reconnection length scale is short compared to the ion skin depth, so Hall terms and electron inertia are important.
6. A model showing that ions experience fast stochastic heating during fast collisionless reconnection (Yoon & Bellan, 2018, 2019b)

7. A model showing how the reverse current associated with coronal mass ejection drives EUV fronts in the solar corona (Wongwaitayakornkul et al., 2019)

5. Summary and Discussion

Laboratory experiments exhibit a wide range of phenomena that are scalable to the solar corona. Because the experiments are real, they automatically incorporate a completely self-consistent set of physics and so, in contrast to analytic or numerical models, do not contain any simplifying assumptions. By using increasingly sophisticated diagnostics and by careful arrangement of initial and boundary conditions, detailed information on a variety of physical phenomena can be obtained. Because the experiments are reproducible and have many controllable parameters, physical models can be quantitatively tested. The discovery of new and unexpected phenomena, such as kink instigation of RTI, stimulates development of new models relevant to the solar situation. Experimentally observed phenomena that are not directly scalable to the solar corona are also useful because these raise questions of how such phenomena might occur in the solar context. Although the experiments scale well to solar situations to the extent that both can be described by ideal MHD, nonideal phenomena typically cannot be directly scaled and may be different. An important difference of this sort involves the separation of scales having different types of physics, for example, the separation between ideal MHD and Hall MHD. In the solar corona this separation of scales is extreme, so that it is difficult to observe the Hall scale which is of the order of meters which is essentially infinitesimal compared to the ideal MHD scale which is millions of meters. The separation of scales between ideal and Hall MHD is much less in the experiment, so it is possible to observe coupling between these scales. Addressing this difference leads to the concept that the solar corona does not have a single ideal MHD scale but rather has a range of ideal MHD scales arranged in a fractal fashion where the very smallest ideal MHD scale couples to the Hall scale. This concept is consistent with the fractal nature of observed solar phenomenon and in particular the property that when resolution is increased the phenomenology remains similar to what was seen at larger scales. A similar issue affects the Lundquist number which just barely satisfies the requirement of being large compared to unity in the experiment but is enormously larger than unity in the solar corona. This means that resistive phenomena cannot be directly scaled from the experiment to the solar corona, but it also means that any effect of finite resistivity is more easily seen. The electron drift velocity relative to ions is a much higher fraction of the Alfvén velocity in the lab experiment than on the Sun, and this means that the threshold for kinetic instability is lower in the experiment. While this again means that the experiment cannot be kinetically scaled to the solar corona, it also means that it is easier to resolve kinetic phenomena in the experiment and so develop an understanding for underlying physics. The laboratory experiments thus provide an important and complementary contribution to the understanding of solar corona physics.

Data Availability Statement

All data are properly cited and can be accessed in the following references: You et al. (2005), Haw and Bellan (2017), Stenson and Bellan (2008), Hansen and Bellan (2001), Ha and Bellan (2016), Wongwaitayakornkul et al. (2017), Haw et al. (2018, 2019), Marshall et al. (2018), Zhang et al. (2020), and Seo et al. (2020)

Acknowledgments

This two decades of experimental research has been supported by grants from the NSF, USDOE, and AFOSR. The most recent are from the NSF/DOE Partnership in Plasma Science and Engineering via USDOE Grant DE-FG02-04ER54755, the Air Force Office of Scientific Research via Award FA9550-11-1-0184, the NSF SHINE program via Award 1059519, and the NSF Solar Terrestrial Research Program via Award 1914599.

References

Alfvén, H. (1986). Double-layers and circuits in astrophysics. *IEEE Transactions on Plasma Science*, *14*(6), 779–793. https://doi.org/10.1109/TPS.1986.4316626

Alfvén, H., & Carlqvist, P. (1967). Currents in the solar atmosphere and a theory of solar flares. *Solar Physics*, *1*(2), 220–228. https://doi.org/10.1007/BF00150857

Bellan, P. M. (2003). Why current-carrying magnetic flux tubes gobble up plasma and become thin as a result. *Physics of Plasmas*, *10*(5), 1999–2008. https://doi.org/10.1063/1.1558275

Bellan, P. M. (2006). *Fundamentals of plasma physics*. Cambridge: Cambridge University Press. https://doi.org/10.1017/CBO9780511807183

Bellan, P. M. (2013). Circular polarization of obliquely propagating whistler wave magnetic field. *Physics of Plasmas*, *20*(8), 082113. https://doi.org/10.1063/1.4817964

Bellan, P. M. (2016a). Integrated accretion disc angular momentum removal and astrophysical jet acceleration mechanism. *Monthly Notices of the Royal Astronomical Society*, *458*(4), 4400–4421. https://doi.org/10.1093/mnras/stw562

Bellan, P. M. (2016b). Revised single-spacecraft method for determining wave vector k and resolving space-time ambiguity. *Journal of Geophysical Research: Space Physics*, *121*, 8589–8599. https://doi.org/10.1002/2016JA022827

Bellan, P. M. (2018a). Experiments relevant to astrophysical jets. *Journal of Plasma Physics*, *84*(5). https://doi.org/10.1017/S0022377818 00079X

Bellan, P. M. (2018b). Experiments and models of MHD jets and their relevance to astrophysics and solar physics. *Physics of Plasmas*, *25*(5), 055601. https://doi.org/10.1063/1.5009571
Bellan, P. M. (2018c). *Magnetic helicity, spheromaks, solar corona loops, and astrophysical jets*. World Scientific (Singapore; Hackensack, NJ). https://doi.org/10.1142/q0151
Bellan, P. M. (2018d). Model for how an accretion disk drives astrophysical jets and sheds angular momentum. *Plasma Physics and Controlled Fusion*, *60*(1), 014006. https://doi.org/10.1088/1361-6587/aa85f9
Bellan, P. M. (2020). Analytic model for the time-dependent electromagnetic field of an astrophysical jet. *The Astrophysical Journal*, *888*(2), 69. https://doi.org/10.3847/1538-4357/ab5f0d
Bellan, P. M., You, S., & Hsu, S. C. (2005). Simulating astrophysical jets in laboratory experiments. In G. A. Kyrala (Ed.), *High Energy Density Laboratory Astrophysics* (pp. 203–209). Berlin/Heidelberg: Springer-Verlag.
Berger, M. A., & Field, G. B. (1984). The topological properties of magnetic helicity. *Journal of Fluid Mechanics*, *147*, 133–148.
Bhattacharjee, A., Ma, Z. W., & Wang, X. (2001). Recent developments in collisionless reconnection theory: Applications to laboratory and space plasmas. *Physics of Plasmas*, *8*(5), 1829–1839. https://doi.org/10.1063/1.1353803
Braginskii, S. I. (1965). Transport processes in a plasma. In M. A. Leontovich (Ed.), *Reviews of plasma physics* (Vol. 1, pp. 205–311) New York: Consultants Bureau.
Calugareanu, G. (1959). L'integrale de Gauss et l'Analyse des noeuds tridimensionnels. *Revue Roumaine des Mathematiques Pures et Appliquees*, *4*, 5.
Chai, K. B., & Bellan, P. M. (2013). Extreme ultra-violet movie camera for imaging microsecond time scale magnetic reconnection. *Review of Scientific Instruments*, *84*(12), 123,504.
Chandrasekhar, S. (1961). *Hydrodynamic and hydromagnetic stability*. *The International series of monographs on physics* (pp. 464). Oxford: Clarendon Press.
Chen, F. F. (1984). *Introduction to plasma physics and controlled fusion*. Boston, MA: Springer US. https://doi.org/10.1007/978-1-4757 - 5595-4
Chen, J. (2003). Acceleration of coronal mass ejections. *Journal of Geophysical Research*, *108*(A11), 1410. https://doi.org/10.1029/2003JA009849
Chen, J., Marque, C., Vourlidas, A., Krall, J., & Schuck, P. W. (2006). The flux rope scaling of the acceleration of coronal mass ejections and eruptive prominences. *The Astrophysical Journal*, *649*(1), 452–463. https://doi.org/10.1086/506466
Dreicer, H. (1959). Electron and ion runaway in a fully ionized gas. I. *Physical Review*, *115*(2), 238–249. https://doi.org/10.1103/PhysRev.115.238
Erdelyi, R., & Goossens, M. (1995). Resonant absorption of Alfven waves in coronal loops in visco-resistive MHD. *Astronomy and Astrophysics*, *294*, 575–586.
Fan, Y. (2017). MHD simulations of the eruption of coronal flux ropes under coronal streamers. *The Astrophysical Journal*, *844*(1), 26. https://doi.org/10.3847/1538-4357/aa7a56
Finn, J. M., & Antonsen, T. M. (1985). Magnetic helicity: What is it, and what is it good for? *Comments on Plasma Physics and Controlled Fusion*, *9*, 111.
Goedbloed, H., Keppens, R., & Poedts, S. (2019). *Magnetohydrodynamics of laboratory and astrophysical plasmas*(1st ed.). Cambridge: University Press. https://doi.org/10.1017/9781316403679
Greene, J. M. (1988). Geometrical properties of three-dimensional reconnecting magnetic fields with nulls. *Journal of Geophysical Research*, *93*(A8), 8583. https://doi.org/10.1029/JA093iA08p08583
Ha, B. N., & Bellan, P. M. (2016). Laboratory demonstration of slow rise to fast acceleration of arched magnetic flux ropes: LABORATORY FLUX ROPES. *Geophysical Research Letters*, *43*, 9390–9396. https://doi.org/10.1002/2016GL069744
Hansen, J. F., & Bellan, P. M. (2001). Experimental demonstration of how strapping fields can inhibit solar prominence eruptions. *The Astrophysical Journal*, *563*(2), L183–L186. https://doi.org/10.1086/338736
Hansen, J. F., Tripathi, S. K. P., & Bellan, P. M. (2004). Co- and counter-helicity interaction between two adjacent laboratory prominences. *Physics of Plasmas*, *11*(6), 3177–3185. https://doi.org/10.1063/1.1724831
Haw, M. A., & Bellan, P. M. (2017). MHD collimation mechanism in arched flux ropes characterized using volumetric, time-dependent B-vector measurements. *Geophysical Research Letters*, *44*, 9525–9531. https://doi.org/10.1002/2017GL074505
Haw, M. A., Seo, B., & Bellan, P. M. (2019). Laboratory measurement of large amplitude whistler pulses generated by fast magnetic reconnection. *Geophysical Research Letters*, *46*, 7105–7112. https://doi.org/10.1029/2019GL082621
Haw, M. A., Wongwaitayakornkul, P., Li, H., & Bellan, P. M. (2018). Reverse current model for coronal mass ejection cavity formation. *The Astrophysical Journal*, *862*(2), L15. https://doi.org/10.3847/2041-8213/aad33c
Hsu, S. C., & Bellan, P. M. (2003). Experimental identification of the kink instability as a poloidal flux amplification mechanism for coaxial gun spheromak formation. *Physical Review Letters*, *90*, 215,002. https://doi.org/10.1103/PhysRevLett.90.215002
Jacobsen, C., & Carlqvist, P. (1964). Solar flares caused by circuit interruptions. *Icarus*, *3*(3), 270–272. https://doi.org/10.1016/0019-1035(64)90023-5
Jensen, T. H., & Chu, M. S. (1984). Current drive and helicity injection. *Physics of Fluids*, *27*, 2881–2885.
Khodachenko, M., Haerendel, G., & Rucker, H. O. (2003). Inductive electromagnetic effects in solar current-carrying magnetic loops. *Astronomy & Astrophysics*, *401*(2), 721–732. https://doi.org/10.1051/0004-6361:20030146
Kliem, B., & Torok, T. (2006). Torus instability. *Physical Review Letters*, *96*(255002). https://doi.org/10.1103/PhysRevLett.96.255002
Klimchuk, J. A. (2000). Cross sectional properties of coronal loops. *Solar Physics*, *193*(1/2), 53–75. https://doi.org/10.1023/A:1005210127703
Kruskal, M., & Schwarzschild, M. (1954). Some instabilities of a completely ionized plasma. *Proceedings of the Royal Society of London Series a-Mathematical and Physical Sciences*, *223*(1154), 348–360. https://doi.org/10.1098/rspa.1954.0120
Kruskal, M., & Tuck, J. L. (1958). The instability of a pinched fluid with a longitudinal magnetic field. *Proceedings of the Royal Society of London Series a-Mathematical and Physical Sciences*, *245*(1241), 222–237. https://doi.org/10.1098/rspa.1958.0079
Kumar, D., & Bellan, P. M. (2009). Nonequilibrium Alfvenic plasma jets associated with spheromak formation. *Physical Review Letters*, *103*, 105,003. https://doi.org/10.1103/PhysRevLett.103.105003
Li, X. B., & Cross, R. C. (1994). Measurement of plasma diamagnetism by a coil located inside a conducting wall. *Review of Scientific Instruments*, *65*(8), 2623–2626. https://doi.org/10.1063/1.1144661
Long, D. M., Bloomfield, D. S., Chen, P. F., Downs, C., Gallagher, P. T., Kwon, R.-Y., et al. (2017). Understanding the physical nature of coronal "EIT waves". *Solar Physics*, *292*(1), 7 English.
Marshall, R. S., & Bellan, P. M. (2019). Acceleration of charged particles to extremely large energies by a sub-Dreicer electric field. *Physics of Plasmas*, *26*(4), 042102. https://doi.org/10.1063/1.5081716

Marshall, R. S., Flynn, M. J., & Bellan, P. M. (2018). Hard X-ray bursts observed in association with Rayleigh-Taylor instigated current disruption in a solar-relevant lab experiment. *Physics of Plasmas*, *25*(11), 112101. https://doi.org/10.1063/1.5054927
Melrose, D. B. (1995). Current paths in the corona and energy release in solar flares. *The Astrophysical Journal*, *451*, 391. https://doi.org/10.1086/176228
Mikkelsen, D. R., White, R. B., Akers, R. J., Kaye, S. M., McCune, D. C., & Menard, J. E. (1997). Energetic particle orbits in the National Spherical Tokamak Experiment. *Physics of Plasmas*, *4*(10), 3667–3675. https://doi.org/10.1063/1.872263
Moffat, H. K. (1978). *Magnetic field generation in electrically conducting fluids*. Cambridge: Cambridge University Press. https://doi.org/10.1017/S002211207923067X
Moser, A. L., & Bellan, P. M. (2012). Magnetic reconnection from a multiscale instability cascade. *Nature*, *482*, 379–381. https://doi.org/10.1038/nature10827
Newcomb, W. A. (1960). Hydromagnetic stability of a diffuse linear pinch. *Annals of Physics*, *10*(2), 232–267. https://doi.org/10.1016/0003-4916(60)90023-3
O'Neil, T. M. (1995). Plasmas with a single sign of charge (an overview). *Physica Scripta*, *T59*, 341–351. https://doi.org/10.1088/0031-8949/1995/T59/047
Ofman, L., Davila, J. M., & Steinolfson, R. S. (1994). Coronal heating by the resonant absorption of Alfven waves: The effect of viscous stress tensor. *The Astrophysical Journal*, *421*, 360. https://doi.org/10.1086/173654
Parker, E. N. (1996). Current paths in the corona and energy release in solar flares—Comment. *Astrophysical Journal*, *471*(1), 489–496. https://doi.org/10.1086/177984
Parker, E. N. (2001). A critical review of Sun-space physics. In N. Meyer-Vernet, M. Moncuquet, & F. Pantellini (Eds.), *Physics of space: Growth points and problems* (pp. 1–11). Dordrecht: Springer Netherlands.
Parker, E. N. (2007). *Conversations on electric and magnetic fields in the cosmos*. Princeton, NJ: Princeton University Press.
Perkins, R. J. (2011). Experimental and analytical studies of merging plasma loops on the Caltech Solar Loop Experiment (PhD thesis), California Institute of Technology.
Peter, H., & Judge, P. G. (1999). On the Doppler shifts of solar ultraviolet emission lines. *The Astrophysical Journal*, *522*(2), 1148–1166. https://doi.org/10.1086/307672
Pfister, H., & Gekelman, W. (1991). Demonstration of helicity conservation during magnetic reconnection using Christmas ribbons. *American Journal of Physics*, *59*, 497–502.
Ryutov, D. D., Drake, R. P., & Remington, B. A. (2000). Criteria for scaled laboratory simulations of astrophysical MHD phenomena. *Astrophysical Journal Supplement Series*, *127*, 465–468. https://doi.org/10.1086/313320
Ryutov, D. D., Remington, B. A., Robey, H. F., & Drake, R. P. (2001). Magnetohydrodynamic scaling: From astrophysics to the laboratory. *Physics of Plasmas*, *8*, 1804–1816. https://doi.org/10.1063/1.1344562
Seo, B., Wongwaitayakornkul, P., Haw, M. A., Marshall, R. S., Li, H., & Bellan, P. M. (2020). Determination of a macro- to micro-scale progression leading to a magnetized plasma disruption. *Physics of Plasmas*, *27*(2), 022109. https://doi.org/10.1063/1.5140348
Shafranov, V. D. (1966). Plasma equilibrium in a magnetic field. *Reviews of Plasma Physics*, *2*, 103.
Shafranov, V. D. (1970). Hydromagnetic stability of a current-carrying pinch in a strong longitudinal magnetic field. *Soviet Physics Technical Physics-USSR*, *15*, 175.
Shibata, K., & Uchida, Y. (1986). Sweeping-magnetic-twist mechanism for the acceleration of jets in the solar atmosphere. *Solar Physics*, *103*(2), 299–310. https://doi.org/10.1007/BF00147831
Stenson, E. V., & Bellan, P. M. (2008). Dual-species plasmas illustrate MHD flows. *IEEE Transactions on Plasma Science*, *36*, 1206–1207. https://doi.org/10.1109/TPS.2008.927095
Stenson, E. V., & Bellan, P. M. (2012). Magnetically driven flows in arched plasma structures. *Physical Review Letters*, *109*, 075001. https://doi.org/10.1103/PhysRevLett.109.075001
Su, Y., & van Ballegooijen, A. (2012). Observations and magnetic field modeling of a solar polar crown prominence. *The Astrophysical Journal*, *757*(2), 168. https://iopscience.iop.org/article/10.1088/0004-637X/757/2/168 https://doi.org/10.1088/0004-637X/757/2/168
Tripathi, S. K. P., Bellan, P. M., & Yun, G. S. (2007). Observation of kinetic plasma jets in a coronal-loop simulation experiment. *Physical Review Letters*, *98*, 135002. https://doi.org/10.1103/PhysRevLett.98.135002
Verkhoglyadova, O. P., Tsurutani, B. T., & Lakhina, G. S. (2010). Properties of obliquely propagating chorus: Obliquely propagating chorus. *Journal of Geophysical Research*, *115*, A00F19. https://doi.org/10.1029/2009JA014809
Woltjer, L. (1958). A theorem on force-free magnetic fields. *Proceedings of the National Academy of Sciences*, *44*(6), 489–491. https://doi.org/10.1073/pnas.44.6.489
Wongwaitayakornkul, P., Haw, M. A., Li, H., & Bellan, P. M. (2019). Magnetically induced current piston for generating extreme-ultraviolet fronts in the solar corona. *The Astrophysical Journal*, *874*(2), 137. https://doi.org/10.3847/1538-4357/ab09f2
Wongwaitayakornkul, P., Haw, M. A., Li, H., Li, S., & Bellan, P. M. (2017). Apex dips of experimental flux ropes: helix or cusp? *The Astrophysical Journal*, *848*(2), 89. https://doi.org/10.3847/1538-4357/aa8990
Wongwaitayakornkul, P., Li, H., & Bellan, P. M. (2020). 3D numerical simulation of kink-driven Rayleigh-Taylor instability leading to fast magnetic reconnection. *The Astrophysical Journal*, *895*(1), L7. https://doi.org/10.3847/2041-8213/ab8e35
Yoon, Y. D., & Bellan, P. M. (2017). A generalized two-fluid picture of non-driven collisionless reconnection and its relation to whistler waves. *Physics of Plasmas*, *24*(5), 052114. https://doi.org/10.1063/1.4982812
Yoon, Y. D., & Bellan, P. M. (2018). Fast ion heating in transient collisionless magnetic reconnection via an intrinsic stochastic mechanism. *The Astrophysical Journal*, *868*(2), L31. https://doi.org/10.3847/2041-8213/aaf0a3
Yoon, Y. D., & Bellan, P. M. (2019a). The electron canonical battery effect in magnetic reconnection: Completion of the electron canonical vorticity framework. *Physics of Plasmas*, *26*(10), 100702. https://doi.org/10.1063/1.5122225
Yoon, Y. D., & Bellan, P. M. (2019b). Kinetic verification of the stochastic ion heating mechanism in collisionless magnetic reconnection. *The Astrophysical Journal*, *887*(2), L29. https://doi.org/10.3847/2041-8213/ab5b0a
You, S., Yun, G. S., & Bellan, P. M. (2005). Dynamic and stagnating plasma flow leading to magnetic-flux-tube collimation. *Physical Review Letters*, *95*, 045002. https://doi.org/10.1103/PhysRevLett.95.045002
Zhai, X. (2015). Experimental, numerical and analytical studies of the MHD-driven plasma jet, instabilities and waves (PhD thesis), California Institute of Technology. Appendix A.
Zhai, X., Li, H., Bellan, P. M., & Li, S. T. (2014). Three-dimensional MHD simulation of the Caltech Plasma Jet Experiment: First results. *Astrophysical Journal*, *791*, 40. https://doi.org/10.1088/0004-637X/791/1/40
Zhang, Y., Wongwaitayakornkul, P., & Bellan, P. M. (2020). Magnetic Rayleigh-Taylor instability in an experiment simulating a solar loop. *The Astrophysical Journal*, *889*(2), L32. https://doi.org/10.3847/2041-8213/ab6b2d